



HAL
open science

Covalent Grafting of Polyoxometalate Hybrids onto Flat Silicon/Silicon Oxide: Insights from POMs Layers on Oxides

Maxime Laurans, Kelly Trinh, Kevin Dalla Francesca, Guillaume Izzet, Sandra Alves, Etienne Derat, Vincent Humblot, Olivier Pluchery, Dominique Vuillaume, Stéphane Lenfant, et al.

► To cite this version:

Maxime Laurans, Kelly Trinh, Kevin Dalla Francesca, Guillaume Izzet, Sandra Alves, et al.. Covalent Grafting of Polyoxometalate Hybrids onto Flat Silicon/Silicon Oxide: Insights from POMs Layers on Oxides. ACS Applied Materials & Interfaces, 2020, 12 (42), pp.48109-48123. 10.1021/ac-sami.0c12300 . hal-03012776

HAL Id: hal-03012776

<https://hal.science/hal-03012776v1>

Submitted on 19 Nov 2020

HAL is a multi-disciplinary open access archive for the deposit and dissemination of scientific research documents, whether they are published or not. The documents may come from teaching and research institutions in France or abroad, or from public or private research centers.

L'archive ouverte pluridisciplinaire **HAL**, est destinée au dépôt et à la diffusion de documents scientifiques de niveau recherche, publiés ou non, émanant des établissements d'enseignement et de recherche français ou étrangers, des laboratoires publics ou privés.

Covalent Grafting of Polyoxometalate Hybrids onto Flat Silicon/Silicon Oxide: Insights from POMs Layers on Oxides

Maxime Laurans, Kelly Trinh, Kevin Dalla Francesca, Guillaume Izzet, Sandra Alves, Etienne Derat, Vincent Humblot, Olivier Pluchery, Dominique Vuillaume, Stéphane Lenfant, Florence Volatron, and Anna Proust

ACS Appl. Mater. Interfaces, **Just Accepted Manuscript** • DOI: 10.1021/acsami.0c12300 • Publication Date (Web): 28 Sep 2020

Downloaded from pubs.acs.org on October 1, 2020

Just Accepted

“Just Accepted” manuscripts have been peer-reviewed and accepted for publication. They are posted online prior to technical editing, formatting for publication and author proofing. The American Chemical Society provides “Just Accepted” as a service to the research community to expedite the dissemination of scientific material as soon as possible after acceptance. “Just Accepted” manuscripts appear in full in PDF format accompanied by an HTML abstract. “Just Accepted” manuscripts have been fully peer reviewed, but should not be considered the official version of record. They are citable by the Digital Object Identifier (DOI®). “Just Accepted” is an optional service offered to authors. Therefore, the “Just Accepted” Web site may not include all articles that will be published in the journal. After a manuscript is technically edited and formatted, it will be removed from the “Just Accepted” Web site and published as an ASAP article. Note that technical editing may introduce minor changes to the manuscript text and/or graphics which could affect content, and all legal disclaimers and ethical guidelines that apply to the journal pertain. ACS cannot be held responsible for errors or consequences arising from the use of information contained in these “Just Accepted” manuscripts.

1
2
3
4
5
6
7
8
9
10
11
12
13
14
15
16
17
18
19
20
21
22
23
24
25
26
27
28
29
30
31
32
33
34
35
36
37
38
39
40
41
42
43
44
45
46
47
48
49
50
51
52
53
54
55
56
57
58
59
60

Covalent Grafting of Polyoxometalate Hybrids onto Flat Silicon/Silicon Oxide: Insights from POMs Layers on Oxides

*Maxime Laurans,^a Kelly Trinh,^{a,d} Kevin Dalla Francesca,^a Guillaume Izzet,^a Sandra Alves,^a Etienne Derat,^a Vincent Humblot,^{c, †} Olivier Pluchery,^d Dominique Vuillaume,^b Stéphane Lenfant,^b Florence Volatron,^a Anna Proust^{*a}*

^aSorbonne Université, CNRS, Institut Parisien de Chimie Moléculaire, IPCM, 4 Place Jussieu, F-75005 Paris, France

^b Institute for Electronics Microelectronics and Nanotechnology (IEMN), CNRS, Av. Poincaré, Villeneuve d'Ascq, France

^c Sorbonne Université, CNRS, Laboratoire de réactivité de surface, LRS, 4 Place Jussieu, F-75005 Paris, France

1
2
3 † present address: FEMTO-ST Institute, UMR CNRS 6174, Université Bourgogne
4
5 Franche-Comté, 15B avenue des Montboucons, 25030 Besançon Cedex, France
6
7
8
9

10
11 † Sorbonne Université, CNRS, Institut des Nanosciences de Paris,
12
13 INSP, 4 Place Jussieu, F-75005 Paris, France
14
15
16
17
18
19
20

21
22 KEYWORDS polyoxometalates, molecular oxides, surface
23
24 functionalization, electron transport, silicon dioxide, covalent
25
26 anchoring
27
28
29

30 ABSTRACT
31
32
33

34 Immobilization of polyoxometalates (POMs) onto oxides is relevant
35
36 to many applications in the fields of catalysis, energy
37
38 conversion/storage or molecular electronics. Optimization and
39
40 understanding the molecule/oxide interface is crucial to
41
42 rationally improve the performance of the final molecular
43
44 materials. We herein describe the synthesis and covalent grafting
45
46 of POM hybrids with remote carboxylic acid functions onto flat
47
48 Si/SiO₂ substrates. Special attention has been paid to the
49
50 characterization of the molecular layer and to the description of
51
52 the POM anchoring mode at the oxide interface through the use of
53
54
55
56
57
58
59
60

1
2
3 various characterization techniques, including ellipsometry, AFM,
4
5 XPS and FTIR. Finally, electron transport properties were probed
6
7 in a vertical junction configuration and energy level diagrams
8
9 have been drawn and discussed in relation with the POM molecular
10
11 electronic features inferred from cyclic-voltammetry, UV-visible
12
13 absorption spectra and theoretical calculations. The electronic
14
15 properties of these POM-based molecular junctions are driven by
16
17 the POM LUMO (d-orbitals) whatever the nature of the tether or the
18
19 anchoring group.
20
21
22
23
24
25
26
27
28
29
30

31 **INTRODUCTION**

32
33
34 Polyoxometalates (POMs) are nanometric molecular oxides made of
35
36 early transition metals in their highest oxidation state. Their
37
38 ability to be reduced with several electrons with minor structural
39
40 changes makes them good electron reservoirs that could play
41
42 important roles in various applications in molecular memories,
43
44 energy storage and energy conversion, catalysis...¹⁻⁹ Some of these
45
46 applications involve the use of oxide electrodes. Indeed, in
47
48 capacitive molecular memories, the molecular floating gate is
49
50 usually deposited onto the silicon channel protected by silicon
51
52 dioxide.^{1,10,11} Thus, the molecules are not perturbed by the channel
53
54
55
56
57
58
59
60

1
2
3 and keep their charge state and physical properties. Furthermore,
4
5 in the field of solar energy conversion, e.g. photovoltaic and
6
7 artificial photosynthesis (proton or CO₂ reduction, water
8
9 oxidation...), nanostructured transparent metal oxide
10
11 semiconductors like ITO, TiO₂, NiO or ZnO, and more recently the
12
13 promising Fe₂O₃ or BiVO₄ semiconductors, often modified by an
14
15 organic dye, are usually used to build photo-electrodes.¹²⁻¹⁶
16
17

18 Exploiting the redox activity of POMs in such applications thus
19
20 requires mastering their deposition on oxide surfaces.
21
22 Furthermore, the control of their organization on the surface is
23
24 an essential and still challenging issue. Indeed, Busche et al.,
25
26 who recently reported the study of POM-based flash memories showed
27
28 that the density of deposited POMs is crucial to control the
29
30 write/erase voltage and switching time.¹ In the energy field, it
31
32 is well known that the activity of dye-sensitized photo-electrodes
33
34 will be maximized if the contact between the active molecules and
35
36 the electrode is optimized, which implies: (i) limiting the
37
38 aggregation of the molecules, (ii) preventing the leaching of the
39
40 molecules during operating conditions, (iii) ensuring a strong
41
42 interaction between the molecules and the electrode to densify the
43
44 molecules at the interface and speed up electron transfers.^{3,17-20}
45
46 An efficient answer to all these points is to covalently attach
47
48 the redox active molecules on the electrode.
49
50
51
52
53
54
55
56
57
58
59
60

1
2
3 Herein we demonstrate the robust and controlled grafting of POM
4 hybrids onto Si/SiO₂ substrates. We chose this oxide for its direct
5 applicability in CMOS (complementary metal-oxide semi-conductor)-
6 compatible devices, but also because very flat Si/SiO₂ substrates
7 are available, which permits the use of numerous characterization
8 techniques to probe the surface and interface. Whereas various
9 strategies have been proposed to covalently anchor POMs on oxide
10 nanoparticles surface²¹⁻²³ or mesoporous silica,²⁴ very few examples
11 describe the grafting of POMs on flat oxide substrates.^{13,25} In
12 these last examples, few attention has been devoted to the control
13 of the density and the characterization of the interface. In the
14 present work, to ensure a strong bond between the POMs and the
15 oxide, the POM hybrids with a pendant carboxylic acid group
16 TBA_{4.4}[PW₁₁O₃₉{Sn(C₆H₄)C≡C(C₆H₄)COOH_{0.6}}] (K^W_{Sn}[COOH]) and
17 TBA_{3.4}[PW₁₁O₃₉{O(SiC₂H₄COOH_{0.8})₂}] (K^W_{Si}[COOH]) have been prepared
18 (TBA = N(C₄H₉)₄⁺, tetrabutylammonium). Molecules containing
19 carboxylic acid moieties were scarcely used to functionalize flat
20 silicon oxide substrates^{26,27} but the use of this anchoring function
21 is recognized as a common way to modify non-planar silica surfaces
22 and other oxides.²⁸⁻³⁰

23
24
25
26
27
28
29
30
31
32
33
34
35
36
37
38
39
40
41
42
43
44
45
46
47
48
49
50
51
52
53
54
55
56
57
58
59
60

Once synthesized, the POM hybrids were deposited on a silicon substrate surmounted by its native SiO₂ layer (hereafter named Si/SiO₂ substrate). Various surface characterization techniques were used to study the features of the monolayer and thorough

1
2
3 attention was devoted to characterize the anchoring mode at the
4
5 interface. To go further, the charge transport through the modified
6
7 substrates was studied at the solid state.
8
9

10 11 12 **EXPERIMENTAL SECTION** 13

14 All chemicals and solvents were purchased from Aldrich or Acros
15
16 and used as received, except for triethylamine and acetonitrile
17
18 that were distilled from CaH₂. The lacunar POM K₇[PW₁₁O₃₉] and the
19
20 hybrid platform TBA₄[PW₁₁O₃₉{SnC₆H₄I}] (K^W_{Sn}[I], TBA = N(C₄H₉)₄⁺,
21
22 tetrabutylammonium) were synthesized following previously reported
23
24 procedures.^{31,32} The silicon wafers (highly phosphorus-doped n-
25
26 Si(100), resistivity <5.10⁻³ Ω.cm) for AFM, XPS and electrical
27
28 characterizations were purchased from Siltronix and the silicon
29
30 wafers for FTIR spectroscopy (Float-zone, low phosphorus-doped n-
31
32 Si(100), resistivity 20-30 Ω.cm) were purchased from Neyco.
33
34
35
36

37 NMR spectra were recorded on a Bruker AvanceIII Nanobay 400 MHz
38
39 spectrometer equipped with a BBFO probehead. ¹H chemical shifts
40
41 are quoted as parts per million (ppm) relative to tetramethylsilane
42
43 using the solvent signals as secondary standard (s: singlet, d:
44
45 doublet, t: triplet, sex: sextet, m: multiplet) and coupling
46
47 constants (J) are quoted in Hertz (Hz). ³¹P chemical shifts are
48
49 quoted relative to 85% H₃PO₄. IR spectrum of the powder was recorded
50
51 from a KBr pellet on a Jasco FT/IR 4100 spectrometer. High-
52
53 resolution ESI mass spectra were recorded using an LTQ Orbitrap
54
55
56
57
58
59
60

1
2
3 hybrid mass spectrometer (ThermoFisher Scientific, Bremen,
4 Germany) equipped with an external ESI source operated in the
5 negative ion mode. Spray conditions included a spray voltage of
6 3.5 kV, a capillary temperature maintained at 270 °C, a capillary
7 voltage of -40 V, and a tube lens offset of -100 V. Sample solutions
8 in acetonitrile ($10 \text{ pmol} \cdot \mu\text{L}^{-1}$) were infused into the ESI source by
9 using a syringe pump at a flow rate of $180 \mu\text{L} \cdot \text{h}^{-1}$. Mass spectra
10 were acquired in the Orbitrap analyzer with a theoretical mass
11 resolving power (R_p) of 100 000 at m/z 400, after ion accumulation
12 to a target value of 10^5 and a m/z range detection from m/z 300 to
13 2000. All data were acquired using external calibration with a
14 mixture of caffeine, MRFA peptide and Ultramark 1600 dissolved in
15 Milli-Q water/ HPLC grade acetonitrile (50/50, v/v). Elemental
16 analyses were performed at the Institut de Chimie des Substances
17 Naturelles, Gif sur Yvette, France. Electrochemical studies were
18 performed on an Autolab PGSTAT 100 workstation (Metrohm) using a
19 standard three-electrode set-up. Glassy carbon electrode, platinum
20 wire and saturated calomel electrode (SCE) were used as the
21 working, auxiliary and reference electrode, respectively. The
22 cyclic voltammograms were recorded in 1 mM solutions of the POMs
23 in acetonitrile with tetrabutylammonium hexafluorophosphate TBAPF_6
24 as electrolyte (0.1 M). UV-visible spectra were recorded on a Cary
25 5000 spectrophotometer.
26
27
28
29
30
31
32
33
34
35
36
37
38
39
40
41
42
43
44
45
46
47
48
49
50
51
52
53
54
55
56
57
58
59
60

Synthesis of TBA_{4.4}[PW₁₁O₃₉{Sn(C₆H₄)C≡C(C₆H₄)COOH_{0.6}}] (K^W_{Sn}[COOH])

K^W_{Sn}[I] (200 mg, 0.050 mmol), 4-ethynylbenzoic acid (14.20 mg, 0.097 mmol), bis(triphenylphosphine) palladium (II) dichloride (2.83 mg, 0.004 mmol) and CuI (1.56 mg, 0.008 mmol) were solubilised in 2 mL of anhydrous DMF preliminary degassed with argon. Then triethylamine (50 μ L, 0.378 mmol) was added. The mixture was degassed for 5 min more before being placed in a microwave oven for 1h at 80°C/80W. After the reaction, solid impurities were observed and removed by centrifugation. Diethyl ether was added to precipitate a powder that was solubilized again in a minimum of acetonitrile. The acetonitrile solution was stirred with TBA⁺ enriched Amberlite[®] ion exchange resin for 1hr. The addition of few drops of ethyl acetate leads to the apparition of a preliminary precipitate that was removed by centrifugation since it contains catalysts residues. The supernatant was then precipitated by further addition of ethyl acetate, K^W_{Sn}[COOH] was recovered by centrifugation and dried with a large excess of diethyl ether to give a yellow pale powder (70-80%).

¹H NMR (400 MHz, CD₃CN): δ (ppm) 8.01 (d, ³J_{H-H}=8.02Hz, 2H, Ar-H), 7.75 (d+dd, ³J_{H-H}=7.74Hz, ³J_{Sn-H}= 93.4 Hz, 2H, Ar-H), 7.66 (d+dd, ³J_{H-H}=7.74Hz, ⁴J_{Sn-H}= 31 Hz, 2H, Ar-H), 7.60 (d, ³J_{H-H}=8.02Hz, 2H, Ar-H), 3.12 (m, 35H, N-CH₂-CH₂-CH₂-CH₃), 1.63 (m, 35H, N-CH₂-CH₂-CH₂-CH₃), 1.39 (sex, ³J_{H-H}=7.74Hz, 35H, N-CH₂-CH₂-CH₂-CH₃), 0.98 (t, ³J_{H-H}=7.74Hz, 53H, N-CH₂-CH₂-CH₂-CH₃); ³¹P NMR (121 MHz, CD₃CN): δ (ppm)

1
2
3 - 10.90 (s+d, $^2J_{\text{Sn-P}}=12.11\text{Hz}$); IR (KBr pellet, cm^{-1}): $\nu=2961$ (m),
4 2934 (m), 2873 (m), 1709(w), 1604(w), 1548 (w), 1483 (m), 1379
5 (w), 1070 (s), 962 (s), 886 (s), 798 (s); HRMS (ESI⁻): m/z: calcd
6 for $\text{PW}_{11}\text{O}_{41}\text{SnC}_{15}\text{H}_9$: 754.30 [M]⁴⁻ ; found 754.30 (100) ; calcd for
7 $\text{PW}_{11}\text{O}_{41}\text{SnC}_{31}\text{H}_{45}\text{N}$: 1086.50 [M + TBA]³⁻ ; found 1086.50 (50) ; calcd
8 for $\text{PW}_{11}\text{O}_{41}\text{SnC}_{15}\text{H}_8$: 603.24 [M]⁵⁻; found 603.24 (25) ; calcd for
9 $\text{PW}_{11}\text{O}_{41}\text{SnC}_{47}\text{H}_{81}\text{N}_2$: 1750.89 [M + 2TBA]²⁻; found 1750.89 (15); Anal.
10 Calcd for $\text{TBA}_{4.4}[\text{PW}_{11}\text{O}_{39}\{\text{Sn}(\text{C}_{14}\text{H}_8)\text{COOH}_{0.6}\}]$ (%): C 25.12, H 4.12, N
11 1.51; found : C 24.80, H 3.92, N 1.54; UV-vis spectroscopy (CH_3CN):
12 λ (nm) ($\log \epsilon$, ϵ in $\text{mol}^{-1}\cdot\text{L}\cdot\text{cm}^{-1}$): 263 (4.73), 283 (4.66), 300 (4.69),
13 319 (4.59)

14 **Synthesis of $\text{TBA}_4[\text{PW}_{11}\text{O}_{39}\{\text{Sn}(\text{C}_6\text{H}_4)\text{C}\equiv\text{C}(\text{C}_6\text{H}_5)\}]$ ($\text{K}_{\text{Sn}}^{\text{W}}[\text{H}]$)**

15 $\text{K}_{\text{Sn}}^{\text{W}}[\text{I}]$ (400 mg, 0.1 mmol), ethynylbenzene (20 μL , 0.18 mmol),
16 bis(triphenylphosphine) palladium (II) dichloride (7 mg, 0.01
17 mmol) and CuI (3 mg, 0.015 mmol) were solubilised in 4 mL of
18 anhydrous DMF preliminary degassed with argon. Then triethylamine
19 (100 μL , 0.756 mmol) was added. The mixture was degassed for 5 min
20 more then left stirring under inert and ambient temperature during
21 one night. TBABr (500 mg, 1.55 mmol) was added to the mixture then
22 an excess of absolute ethanol to precipitate the product. A solid
23 was recovered by centrifugation, washed with absolute ethanol and
24 diethyl ether. To optimize the number of TBA counter-cations, the

1
2
3 solid was solubilized in the minimum of acetonitrile, and stirred
4
5 with TBA⁺ enriched Amberlite[®] ion exchange resin for 1hr. After
6
7 filtration, the filtrate was precipitated with ether and the solid
8
9 recovered by a last centrifugation. K^W_{Sn}[H] was obtained with a 60%
10
11 yield.
12

13
14 ¹H NMR (400 MHz, CD₃CN): δ (ppm) 7.76 (d+dd, ³J_{H-H}=8.2Hz, ³J_{Sn-H}= 95
15
16 Hz, 2H, Ar-H), 7.65 (d+dd, ³J_{H-H}=8.2Hz, ⁴J_{Sn-H}= 32 Hz, 2H, Ar-H), 7.6
17
18 (m, 2H, Ar-H), 7.45 (m, 3H, Ar-H), 3.16 (m, 32H, N-CH₂-CH₂-CH₂-
19
20 CH₃), 1.66 (m, 32H, N-CH₂-CH₂-CH₂-CH₃), 1.42 (sex, ³J_{H-H}=7.3Hz, 32H,
21
22 N-CH₂-CH₂-CH₂-CH₃), 1.01 (t, ³J_{H-H}=7.3Hz, 48H, N-CH₂-CH₂-CH₂-CH₃); ³¹P
23
24 NMR (121 MHz, CD₃CN): δ (ppm) - 10.9 (s+d, ²J_{Sn-P}=12.15Hz); IR (KBr
25
26 pellet, cm⁻¹): ν=2962 (m), 2931 (m), 2869 (m), 1626(w), 1597(vw),
27
28 1483 (m), 1380 (w), 1069 (s), 961 (s), 885 (s), 798 (s); HRMS (ESI⁻
29
30): m/z: calcd for PW₁₁O₃₉SnC₁₄H₉ : 743.30 [M]⁴⁻ ; found 743.30 (100)
31
32 ; calcd for PW₁₁O₃₉SnC₁₄H₁₀ : 991.41 [M+H]³⁻ ; found 991.41 (70) ;
33
34 calcd for PW₁₁O₃₉SnC₃₀H₄₆N : 1608.25 [M + H + TBA]²⁻ ; found 1608.26
35
36 (30) ; calcd for PW₁₁O₃₉SnC₃₀H₄₅N : 1071.83 [M + TBA]³⁻ ; found 1071.83
37
38 (20); calcd for PW₁₁O₃₉SnC₄₆H₈₁N₂: 1028.89 [M + 2TBA]²⁻; found 1028.90
39
40 (15) Anal. Calcd for PW₁₁O₃₉SnC₇₈H₁₅₃N₄ (%): C 23.75, H 3.88, N 1.42;
41
42 found: C 23.68, H 3.69, N 1.01; UV-vis spectroscopy (CH₃CN): λ
43
44 (nm) (logε, ε in mol⁻¹.L.cm⁻¹): 271 (5.15), 278 (5.13), 285 (5.11),
45
46 304 (4.87).
47
48
49
50
51
52
53
54
55
56
57
58
59
60

Synthesis of $\text{TBA}_{3.4}[\text{PW}_{11}\text{O}_{39}\{\text{O}(\text{SiC}_2\text{H}_4\text{COOH}_{0.8})_2\}] (\text{K}^{\text{W}}_{\text{Si}}[\text{COOH}])$

$\text{K}_7[\text{PW}_{11}\text{O}_{39}]$ (0.64 g, 0.2 mmol) was dissolved in a water/acetonitrile mixture (30 mL, 1:2). A 1 M HCl aqueous solution was added drop by drop until an apparent pH equals to 3. The solution was cooled in an ice bath and the $\text{Si}(\text{OH})_3(\text{CH}_2)_2\text{COONa}$ (0.476 mL, 0.8 mmol) was inserted. The 1 M HCl solution was added drop by drop again to reach $\text{pH}_{\text{app}}=2$. After an overnight reaction, TBABr (0.26 g, 0.8 mmol) was added and the solution concentrated with a rotary evaporator to precipitate the product. The oily compound obtained was dissolved in the minimum of acetonitrile then precipitated again with an excess of ether. A sticky solid was recovered by centrifugation and washed thoroughly with ether to obtain a white powder (0.6 g, 82%).

^1H NMR (400 MHz, CD_3CN): δ (ppm) 3.14 (m, 27H), 2.53 (m, 4H), 1.65 (m, 27H), 1.41 (sex, $^3\text{J}(\text{H},\text{H})=7.5$ Hz, 27H), 1.05 (m, 4H), 1.01 (t, $^3\text{J}(\text{H},\text{H})=7.5$ Hz, 41H), 0.90 (m, 4H); ^{31}P NMR (121 MHz, CD_3CN) δ (ppm) -12.28; IR (KBr pellet, cm^{-1}): $\nu = 2963$ (s), 2935 (m), 2874 (w), 1710 (s), 1623 (w), 1483 (s), 1471 (s), 1420 (w), 1381 (m), 1112 (vs), 1064 (vs), 1052 (s), 1036 (s), 964 (vs), 870 (vs), 824 (vs); HRMS (ESI-), m/z (%) : calcd for $\text{W}_{11}\text{PSi}_2\text{O}_{44}\text{C}_6\text{H}_{10}$: 965.41 $[\text{M}]^{3-}$; found : 965.42 (100) ; calcd for $\text{W}_{11}\text{PSi}_2\text{O}_{44}\text{C}_{22}\text{H}_{46}\text{N}$: 1569.26 $[\text{M}+\text{TBA}]^{2-}$; found: 1569.27 (50) ; calcd for $\text{W}_{11}\text{PSi}_2\text{O}_{44}\text{C}_{22}\text{H}_{45}\text{N}$: 1045.84 $[\text{M} + \text{TBA}]^{3-}$; found : 1045.84 (10) ; calcd for $\text{W}_{11}\text{PSi}_2\text{O}_{44}\text{C}_{38}\text{H}_{81}\text{N}_2$: 1569.27 $[\text{M} +$

1
2
3 2TBA]²⁻; found 1569.26 (8); Elemental Analysis calcd for
4
5 TBA_{3.4}[PW₁₁O₃₉{O (SiC₂H₄COOH_{0.8})₂}] (%): C 19.50, H 3.55, N 1.28;
6
7 found: C 19.51, H 3.50, N 1.24; UV-vis spectroscopy (CH₃CN): λ
8
9 (nm) (logε, ε in mol⁻¹.L.cm⁻¹): 265 (5.59)
10
11
12
13
14

15 **Surface grafting**

16
17 The silicon substrate (1 cm² approximately) was first rinsed with
18
19 a dichloromethane flow then dried under N₂. It was then treated by
20
21 sonication in a basic piranha bath NH₄OH/H₂O₂/H₂O (1/1/2 vol.)
22
23 during 10 min. The treatment was repeated two more times, with
24
25 deionized water rinse between each bath. The substrate was then
26
27 rinsed by immersion in two successive deionized water baths under
28
29 sonication during 5 min. After a thorough drying with N₂ flow, the
30
31 substrate was immersed in an acetonitrile solution of the POM
32
33 hybrid (1 mmol.L⁻¹) and heated at the reflux of the solvent during
34
35 22-24h. The modified substrate was rinsed following the following
36
37 procedure: 5 min sonication in pure acetonitrile / rinsing with
38
39 acetonitrile flow / 5 min sonication in a solution of 0.1 M of
40
41 TBAPF₆ in acetonitrile / rinsing with acetonitrile flow / 5 min
42
43 sonication in pure acetonitrile. The surface was finally rinsed
44
45 with a last flow of acetonitrile before being dried with N₂. This
46
47 rinsing sequence could be repeated once or twice depending on the
48
49 ellipsometry results.
50
51
52
53
54
55
56
57
58
59
60

Ellipsometry

Monowavelength ellipsometer SENTECH SE 400 equipped with a He-Ne laser at $\lambda = 632.8$ nm was used to perform ellipsometry measurements. The incident angle was 70° . The values $n_s = 3.875$ and $k_s = 0.018$ were taken for the silicon wafer, $n_s = 1.5$ and $k_s = 0$ for the SiO_2 layer and $n_s = 1.48$ and $k_s = 0$ for the layer of POMs.^{33,34} The thickness of the SiO_2 layer was estimated by doing a measurement by ellipsometry after the bare silicon substrate rinsing steps, just before immersing the substrate in the POM solution. The thickness of the POM layer was deduced by the subtraction of the SiO_2 layer thickness to the final thickness. At each step, 5 measurements were performed on the substrate in different zones, to check the homogeneity of the layer. A mean value for the thickness was calculated when the standard deviation was lower than 0.2 nm.

Atomic Force Microscopy (AFM)

AFM images were recorded using a commercial AFM (NanoScope VIII MultiMode AFM, Bruker Nano Inc., Nano Surfaces Division, Santa Barbara, CA) equipped with a $150 \times 150 \times 5$ μm scanner (J-scanner). The substrates were fixed on a stainless steel sample puck using a small piece of adhesive tape. Images were recorded in peak force tapping mode in air at room temperature (22–24 °C) using oxide-sharpened microfabricated Si_3N_4 cantilevers (Bruker Nano Inc., Nano

1
2
3 Surfaces Division, Santa Barbara, CA). The spring constants of the
4
5 cantilevers were measured using the thermal noise method, yielding
6
7 values ranging from 0.4 to 0.5 N/m. The curvature radius of
8
9 silicon nitride tips was about 10 nm (manufacturer specifications).
10
11 The raw data were processed using the imaging processing software
12
13 NanoScope Analysis, mainly to correct the background slope between
14
15 the tip and the surfaces.
16
17
18
19
20

21 **X-ray Photoelectron Spectroscopy (XPS)**

22
23 XPS analyses were performed using an Omicron Argus X-ray
24
25 photoelectron spectrometer. The monochromated AlK α radiation
26
27 source ($h\nu = 1486.6$ eV) had a 300 W electron beam power. The
28
29 emission of photoelectrons from the sample was analyzed at a
30
31 takeoff angle of 90° under ultra-high vacuum conditions ($\leq 10^{-}$
32
33 10 Torr). Spectra were carried out with a 100 eV pass energy for
34
35 the survey scan and 20 eV pass energy for the C1s, O1s, N1s, Si
36
37 2p, P 2p, W 4f, Sn 3d, Pd 3d regions. Binding energies were
38
39 calibrated against the Si2p binding energy at 99.4 eV and element
40
41 peak intensities were corrected by Scofield factors. The spectra
42
43 were fitted using Casa XPS v.2.3.15 software (Casa Software Ltd.,
44
45 U.K.) and applying a Gaussian/Lorentzian ratio G/L equal to 70/30.
46
47
48
49
50
51
52

53 **Fourier Transform Infra Red (FTIR) spectroscopy on silicon**

1
2
3 FTIR spectra were recorded with a Bruker Tensor 27 spectrometer,
4 equipped with a DTGS detector, at a resolution of 4 cm^{-1} . Detection
5 was performed in transmission at an incident angle of 70° (Brewster
6 angle for the air-silicon interface) in order to minimize the
7 interferometric patterns in the spectra. Sample compartment is
8 purged from water vapor with a commercial air-dryer (relative
9 humidity around 7%). The silicon substrates are chosen to be float-
10 zone grown and lightly doped in order to have a very low amount of
11 inserted oxygen and to be transparent for the mid-IR wavelengths
12 used in this study.
13
14
15
16
17
18
19
20
21
22
23
24
25
26
27

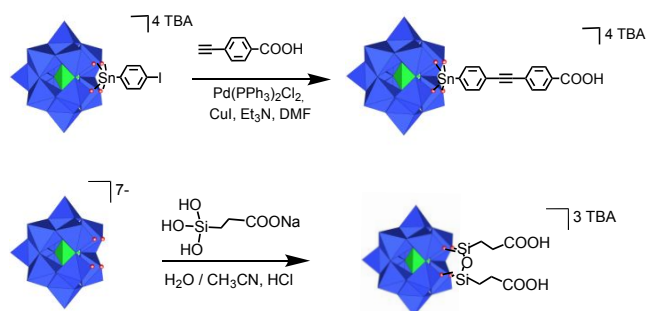
28 **I-V measurements**

29
30 Current-voltage (I-V) curves were measured by contacting the POM
31 monolayer by a Hg drop acting as the top electrode in a glove box
32 filled under a nitrogen flow. The drop was gently brought into
33 contact with the sample surface thanks to a camera. The voltage V
34 was applied on the Hg drop and the highly doped silicon substrate
35 is grounded through the ammeter to measure the current. I-V traces
36 were acquired at different locations (around 10) on the POM
37 monolayer surface, with ~ 5 traces per location, and they were not
38 averaged. The surface contact area is estimated with the camera
39 for each drop formed. Surfaces measured by this approach are
40 comprised in the range $2 - 5 \times 10^{-4}\text{ cm}^2$.
41
42
43
44
45
46
47
48
49
50
51
52
53
54
55
56
57
58
59
60

RESULTS AND DISCUSSION

Synthesis of carboxylic acid terminated POMs

The POM hybrid $\text{TBA}_{4.4}[\text{PW}_{11}\text{O}_{39}\{\text{Sn}(\text{C}_6\text{H}_4)\text{C}\equiv\text{C}(\text{C}_6\text{H}_4)\text{COOH}_{0.6}\}]$ (hereafter named $\text{K}_{\text{Sn}}^{\text{W}}[\text{COOH}]$) was synthesized (see experimental section) by post-functionalization of the hybrid platform $\text{TBA}_4[\text{PW}_{11}\text{O}_{39}\{\text{SnC}_6\text{H}_4\text{I}\}]$ ($\text{K}_{\text{Sn}}^{\text{W}}[\text{I}]$) via a Sonogashira coupling, following a procedure now well mastered in our group (scheme 1).³¹



Scheme 1. Synthetic route to the carboxylic acid terminated hybrids $\text{K}_{\text{Sn}}^{\text{W}}[\text{COOH}]$ (top) and $\text{K}_{\text{Si}}^{\text{W}}[\text{COOH}]$ (bottom).

Fortunately, the coordinating carboxylic acid function of the reactant did not poison the catalyst and the POM hybrid was obtained as a yellow powder with a good yield (80%). $\text{K}_{\text{Sn}}^{\text{W}}[\text{COOH}]$ was characterized by NMR and IR spectroscopies, mass spectrometry and elemental analyses (Figures S1-S4). On the ¹H NMR spectrum, the two typical doublet pairs of the phenyl groups integrating for 2 protons appear at $\delta=7.74$ and $\delta=7.66$ ppm for the phenyl group linked to the inorganic core of the POM, and at $\delta=8.01$ and $\delta=7.60$ ppm for the phenyl group modified with the carboxylic acid function. The

1
2
3 peaks corresponding to the tetrabutylammonium (TBA) cations are
4
5 also present but the integration of the peaks does not correspond
6
7 to 4TBA counter cations as expected with a pure carboxylic acid
8
9 POM hybrid. More TBA cations are present around the POM hybrid,
10
11 which means that a partial amount of POMs is in the carboxylate
12
13 form. This is confirmed by the IR study that shows, in addition to
14
15 the band at 1709cm^{-1} corresponding to the stretching vibration of
16
17 the C=O bond of carboxylic acid function, a band at 1548 cm^{-1} that
18
19 can be attributed to the asymmetric vibration of a carboxylate
20
21 group. The corresponding symmetric vibration band expected around
22
23 $1420\text{-}1335\text{ cm}^{-1}$ is probably hidden in the TBA bands at 1480 and 1380
24
25 cm^{-1} . The carboxylate form is confirmed by the observation of the
26
27 non-majority peak at $m/z = 603.24$ on the mass spectrum, interpreted
28
29 by the presence of a species charged five minus of formula
30
31 $\text{C}_{15}\text{H}_8\text{O}_{41}\text{SnPW}_{11}$. Finally, elemental analysis complies with the
32
33 following formula: $\text{TBA}_{4.4}[\text{PW}_{11}\text{O}_{39}\{\text{Sn}(\text{C}_6\text{H}_4)\text{C}\equiv\text{C}(\text{C}_6\text{H}_4)\text{COOH}_{0.6}\}]$ from
34
35 which we can conclude that in the powder, 30% of the molecules are
36
37 in the carboxylate form whereas 70% are in the carboxylic acid
38
39 form.
40
41
42
43
44
45

46 The cyclic voltammogram (CV) of $\text{K}^{\text{W}}_{\text{Sn}}[\text{COOH}]$ (10^{-3} M) was recorded
47
48 in a $0.1\text{M TBAPF}_6 / \text{acetonitrile}$ solution. The CV recorded at 100
49
50 $\text{mV}\cdot\text{s}^{-1}$ shows three reversible reduction waves at $E_{1/2}=-1.01$ (E_1), $-$
51
52 1.48 (E_2) and -1.64 V (E_3) vs saturated calomel electrode (SCE).
53
54 The value of the two first reduction processes are in accordance
55
56
57
58
59
60

with that reported for other tin derivatives in this family of polyoxotungstates (figure 1) and correspond to successive W(VI) to W(V) one-electron reduction processes.³⁵

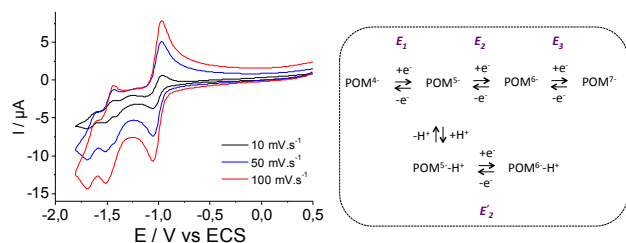


Figure 1. (left) cyclic voltammogram of $K_{Sn}^W[COOH]$ in acetonitrile with $TBAPF_6$ 0.1 M at various scan rates ; $100 \text{ mV}\cdot\text{s}^{-1}$ (red curve) ; $50 \text{ mV}\cdot\text{s}^{-1}$ (blue curve) ; $10 \text{ mV}\cdot\text{s}^{-1}$ (black curve) ; (right) scheme of the mechanism of successive electron and proton transfers. $POM^{4-} = [PW_{11}O_{39}\{Sn(C_6H_4)C\equiv C(C_6H_4)COOH\}]^{4-}$ (potentials are referenced to saturated calomel electrode, add 382 mV to convert to the $Fc^{+/0}$ scale.³⁶

However, on the second reduction wave, a slight inflexion is observed. To better understand its origin we recorded CVs at various scan rates and observed that: at low scan rate ($50 \text{ mV}\cdot\text{s}^{-1}$ and below), the inflexion becomes a full wave at around -1.4 V vs SCE (E'_2 , figure 1); at a scan rate higher than $100 \text{ mV}\cdot\text{s}^{-1}$, the inflexion disappears (figure S5). We propose that after the first reduction process the formed " POM^{5-} " becomes more basic and undergoes intra or intermolecular protonation from a carboxylic acid group. The protonated " $POM^{5-}-H^+$ " is thus more easily reduced and the wave E'_2 corresponds to the reduction potential of a portion of POMs that are protonated (figure 1).³⁷ The second reduction wave

1
2
3 of this "POM⁵⁻-H⁺" species is probably hidden in the second or third
4
5 reduction waves of the unprotonated "POM⁴⁻". As the protonation
6
7 reaction is slower than the electron transfer,³⁸ a portion of the
8
9 "POM⁵⁻" have time to be protonated then reduced at low scan rate
10
11 whereas at a scan rate high enough, only the reduction of the
12
13 unprotonated "POM⁵⁻" occurs.
14
15

16
17 The POM hybrid TBA_{3,4}[PW₁₁O₃₉{O(SiC₂H₄COOH_{0,8})₂}] (hereafter named
18
19 K^W_{Si}[COOH]) was also synthesized (see experimental section), by
20
21 adapting a published procedure.³⁹ This POM is quite different from
22
23 the precedent since it displays aliphatic tethers, two anchoring
24
25 groups and a total charge of -3 that should induce different
26
27 electrochemical properties. It was prepared by a condensation of
28
29 the carboxyethylsilanetriol on the lacunar POM K₇[PW₁₁O₃₉] (figure
30
31 1) in acidic acetonitrile-water. NMR, infrared spectroscopies and
32
33 mass spectrometry confirmed the obtaining of the expected species,
34
35 in particular by the presence on the ¹H NMR spectrum of both
36
37 multiplets at 1.06 and 2.53 ppm integrating for 4 protons
38
39 corresponding to the protons on the aliphatic chains of the POM
40
41 hybrid (figure S6-S9). The excess of TBA cations measured by NMR
42
43 spectroscopy and two contributions in the mass spectrometry
44
45 spectrum again shows that deprotonated species are present, which
46
47 is confirmed by elemental analysis that complies with the following
48
49 general formula: TBA_{3,4}[PW₁₁O₃₉{O(SiC₂H₄COOH_{0,8})₂}]. On the CV of the
50
51 K^W_{Si}[COOH] recorded in a 1 mM solution in acetonitrile with TBAPF₆
52
53
54
55
56
57
58
59
60

1
2
3 (0.1M), the two first one electron reduction waves can be observed
4
5 at $E_{1/2} = -0.38$ and -0.88 V versus SCE in accordance with other Keggin
6
7 type silicon derivatives reported in the literature.⁴⁰ The
8
9 following waves at lower potentials are ill-defined probably due
10
11 to the presence of the COOH functions (figure S10) but no study on
12
13 their dependence upon the scan rate was carried out in this case.
14
15 As expected, the $K_{Si}^W[COOH]$, less charged, is easier to reduce than
16
17 the $K_{Sn}^W[COOH]$.
18
19
20
21
22

23 **UV-visible spectra and DFT calculations**

24
25 The UV-visible spectra of $K_{Si}^W[COOH]$, $K_{Sn}^W[COOH]$ and the reference
26
27 compound (without any functional group)
28
29 $TBA_4[PW_{11}O_{39}\{Sn(C_6H_4)C\equiv C(C_6H_5)\}]$ ($K_{Sn}^W[H]$), recorded in acetonitrile
30
31 solution, are shown on Figure 2. All display the oxygens to
32
33 metal(VI) charge transfer bands characteristic of POMs around 265
34
35 nm and below. In the case of $K_{Sn}^W[COOH]$ and $K_{Sn}^W[H]$ additional
36
37 absorptions are observed at lower energies and are related to the
38
39 conjugated organic chain. All together these electronic
40
41 absorptions disclose the presence of a set of low-lying empty
42
43 orbitals, which might be involved in the charge transport (see
44
45 below).
46
47
48
49
50
51
52
53
54
55
56
57
58
59
60

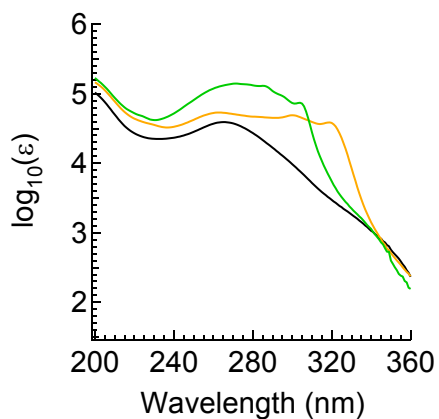


Figure 2. UV visible spectra of $K^W_{Si}[COOH]$ (black), $K^W_{Sn}[COOH]$ (orange) and $K^W_{Sn}[H]$ (green), recorded in acetonitrile.

To gain more insights into their relative energies and the nature of the allowed electronic transitions, DFT and TD-DFT calculations have been undertaken, using the Turbomole package, version 6.4.⁴¹ First of all, two model systems were selected: one corresponding to $K^W_{Si}[COOH]$ and one corresponding to $K^W_{Sn}[COOH]$. In the case of $K^W_{Sn}[COOH]$, we chose to remove the carboxylic acid on the organic moiety for performing the calculations since the protonation state is unclear and we took $K^W_{Sn}[H]$ as a model compound. Geometrical optimization for both systems was conducted at the B3LYP-D3/def2-SV(P) level, with solvation taken into account by adding a continuum solvation model (namely COSMO, with a dielectric constant of 48). A summary of the frontier orbitals for the two calculated systems can be found in Figures 3 and 4 for $K^W_{Si}[COOH]$ and $K^W_{Sn}[H]$ respectively. For $K^W_{Si}[COOH]$, its orbital diagram is

1
2
3 characterized by the following: the HOMO is localized on the sigma
4 system of the two carboxylic acid interacting one with each other
5 (in blue boxes on Figure 3). Four relatively similar orbitals of
6 this type can be found (HOMO, HOMO-1, HOMO-3, HOMO-5). Another
7 block of occupied frontier orbitals can be characterized by
8 oxygens' lone pairs located on the polyoxometalate part of the
9 system (red boxes on Figure 3). The lowest unoccupied molecular
10 orbitals (LUMOs) are characterized by tungsten d orbitals of the
11 polyoxometalate (green boxes on Figure 3). Just above these
12 orbitals can also be found antibonding π orbitals corresponding to
13 the WO oxo bond (purple boxes on Figure 3).
14
15
16
17
18
19
20
21
22
23
24
25
26
27
28
29
30
31
32
33
34
35
36
37
38
39
40
41
42
43
44
45
46
47
48
49
50
51
52
53
54
55
56
57
58
59
60

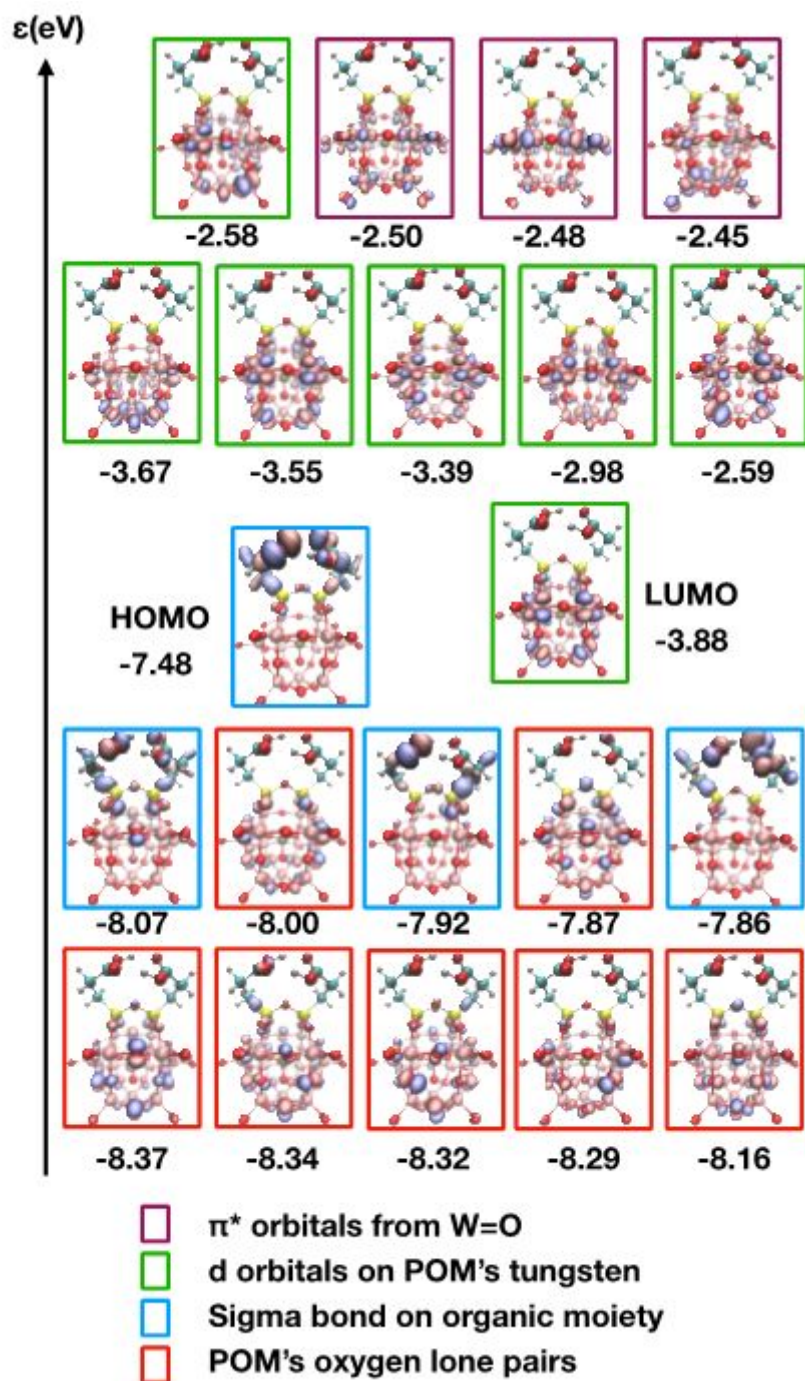


Figure 3. Frontier molecular orbitals for $K^W_{Si}[COOH]$, calculated at the B3LYP-D3/def2-SV(P). Color boxes indicates similar types of orbitals.

Regarding $K^W_{Sn}[H]$, the set of frontiers orbitals is slightly different. HOMO to HOMO-4 can be easily characterized as π orbitals

1
2
3 localized on the organic moiety of the hybrid (black boxes on
4 Figure 4). Just below these five orbitals, one can find the usual
5
6 oxygens' lone pairs located on the polyoxometalate part of the
7
8 system (red boxes on Figure 4). The lowest unoccupied orbitals for
9
10 $K_{Sn}^W[H]$ are similar to those of $K_{Si}^W[COOH]$: first a block of six
11
12 orbitals corresponding to combination of tungsten d orbitals
13
14 (green boxes on Figure 4) followed by antibonding π orbitals
15
16 corresponding to the oxo bond between tungsten and oxygen (purple
17
18 boxes on Figure 4).
19
20
21
22
23
24
25
26
27
28
29
30
31
32
33
34
35
36
37
38
39
40
41
42
43
44
45
46
47
48
49
50
51
52
53
54
55
56
57
58
59
60

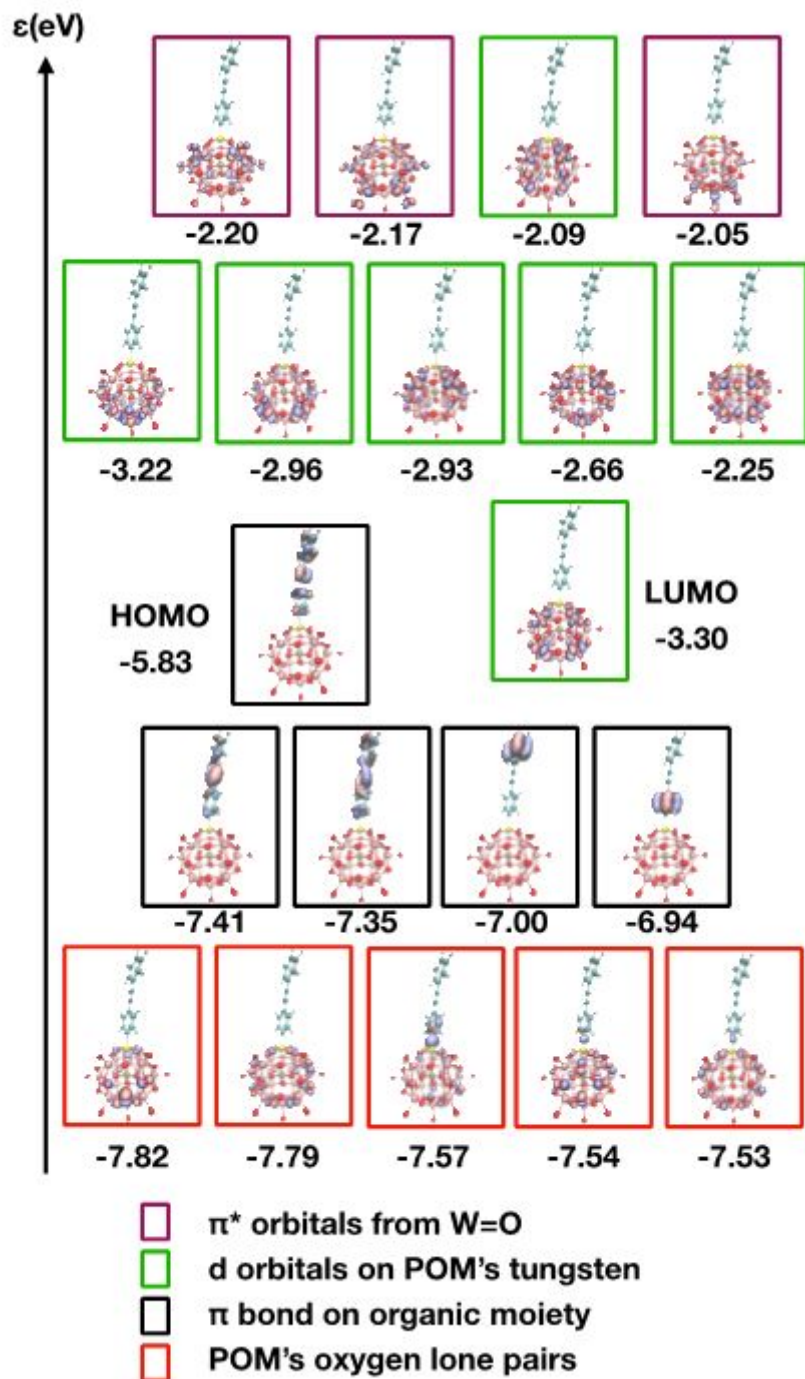


Figure 4. Frontier molecular orbitals for $K^W_{Sn}[H]$, calculated at the B3LYP-D3/def2-SV(P). Color boxes indicates similar types of orbitals.

TD-DFT calculations were then performed to obtain electronic transition attribution. As seen experimentally, the UV spectrum of

1
2
3 $K_{Si}^W[COOH]$ present a major band around 265 nm. This band is properly
4 reproduced by TD-DFT calculations (band A on Figure 5) and is
5 attributed as expected to an electronic transition between
6 oxygens' lone pair towards metal d orbitals. In the case of $K_{Sn}^W[H]$,
7 the same band can be found (band B on Figure 5) involving similar
8 orbital contributions. But, on top of that, we can also attribute
9 the band observed experimentally around 320 nm. From our
10 calculations, it appears that this band can be attributed to a
11 transition between the π system localized on the organic moiety of
12 $K_{Sn}^W[H]$ and d orbitals of POM's tungstens (band C on Figure 5).
13 Because it involves the π system, the position of this band is
14 expected to be sensitive to the functionalization of the aryl unit,
15 as observed experimentally (see Figure 2). The intensity of the
16 calculated band is stronger than expected, which can be attributed
17 to an overestimation of the oscillator strength involving extended
18 conjugated system as previously noted by Tozer.⁴²

19
20
21
22
23
24
25
26
27
28
29
30
31
32
33
34
35
36
37
38
39
40 In conclusion, the computational study gives some insights about
41 the assignment of the main electronic transitions and confirms
42 that the lowest unoccupied molecular orbitals are combination of
43 tungsten d orbitals without any participation of the organic
44 tether.

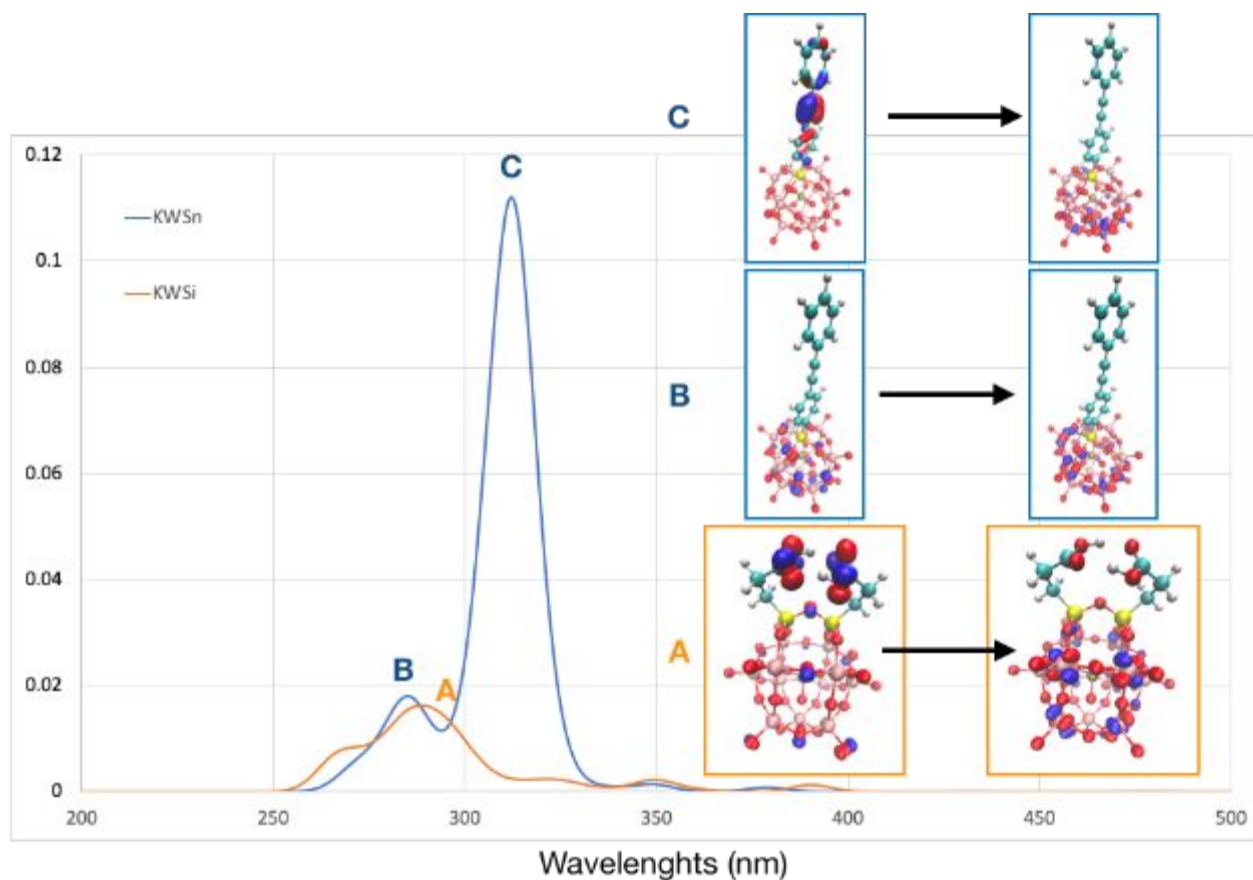


Figure 5. Theoretical UV-visible spectra for $K^{W}_{Sn}[H]$ and $K^{W}_{Si}[COOH]$, calculated at the B3LYP-D3/def2-SV(P) level. Inserts: main orbital contribution for selected electronic transitions.

Grafting on silicon oxide

As mentioned in the introduction, whereas a huge literature exists about the deposition of POM films on oxide substrates by layer-by-layer,^{16,43,44} spin coating,^{15,45} or dip coating on positively charged organic monolayers,^{19,46} involving Van der Waals or electrostatic interactions between the POMs and the substrate, only two examples reported the covalent bonding of POMs on flat oxide substrates. M. Tountas et al. described the insertion of

1
2
3 *tert*-butyl silanol functionalized trivacant Keggin-type POMs
4
5 (TBA)₃[PW₉O₃₄(*t*BuSiOH)₃] in a polymer solar cell at the metal oxide
6
7 (TiO₂ or ZnO) / organic interface.²⁵ Interestingly, the authors
8
9 proposed that strong POM-Si-O-metal bonds were formed at the oxide
10
11 surface via the silanol groups inducing the formation of more
12
13 homogeneous films and the passivation of the metal oxide surface
14
15 stabilizing the system. This new type of interaction at the
16
17 interface contributed to the improvement of the device. E. A.
18
19 Gibson and J. Fielden and coll. reported the study of pristine and
20
21 organo-imido Lindqvist-type POM hybrids (with carboxylic acid and
22
23 pyridine pendant group) as co-adsorbents in dye sensitized p-type
24
25 NiO solar cells.¹³ They showed that the presence of the POMs at
26
27 best slightly improves the overall cell efficiency despite a
28
29 significant increase of V_{oc}. This was attributed to the combination
30
31 of opposite effects such as retardation of both recombination to
32
33 NiO and electron transfer to the electrolyte. Furthermore, no clear
34
35 effect of the nature of the POM was observed. Specially, we could
36
37 expect the POM hybrids with a pendant carboxylic acid function to
38
39 induce a different behavior because of a strong anchoring to the
40
41 NiO surface, albeit no experimental evidence was provided. One
42
43 possible explanation is that the covalent grafting is not
44
45 guaranteed in this study: the POMs layer is indeed added in a
46
47 second step after prior coverage of the substrate by the dye
48
49 sensitizer, also with a carboxylic acid anchor, which could hinder
50
51
52
53
54
55
56
57
58
59
60

1
2
3 the subsequent interaction between the POMs and the oxide
4 substrate.
5

6
7 Here, we chose to deposit the $K_{Sn}^W[COOH]$ and $K_{Si}^W[COOH]$ POM hybrids
8 on Si/SiO₂, a very flat substrate, to have access to crucial surface
9 characterization techniques, such as ellipsometry and AFM, to gain
10 insights into the POM layer features. According to the literature,
11 to ensure a strong bonding between the carboxylic acid and the
12 oxide surface, an annealing step is required.²⁸ Thus in the present
13 case, the deposition was done by heating at the solvent reflux an
14 acetonitrile solution of the POMs containing the freshly cleaned
15 Si/SiO₂ substrate for 24h. The substrate was then rinsed
16 thoroughly, by sonication baths in pure acetonitrile but also in
17 a solution of TBAPF₆ in acetonitrile to eliminate any POM
18 electrostatically deposited.
19
20
21
22
23
24
25
26
27
28
29
30
31
32
33

34
35 The substrate with the $K_{Sn}^W[COOH]$ layer was first characterized
36 by ellipsometry. Theoretically, thicknesses between 2.7 and 3.6 nm
37 are expected (figure 6a). Indeed, the length of the rigid organic
38 arm is around 1.6 nm, the POMs size is 1 nm and the size of the
39 flexible TBA counter cation can vary between 0.5 and 1 nm, as a
40 function of its folding. If we consider molecules standing up-
41 right in the normal direction to the surface with extended TBA, we
42 expect a maximal thickness of 3.6 nm. If tilted molecules with the
43 classical tilt angle of 30° are considered, the minimal expected
44 thickness is 2.7 nm. Based on our statistics (figure S11), we
45
46
47
48
49
50
51
52
53
54
55
56
57
58
59
60

defined 2.3 nm as the lower acceptable limit. Over 17 samples, a majority (60%) gave satisfying thicknesses (between 2.3 and 3.9 nm, Figure S11 in the supporting information) and were regarded as monolayers. The samples obtained with a thickness below 2.3 nm and above 4 nm were regarded as sub-monolayers and multilayers respectively and were sidelined.

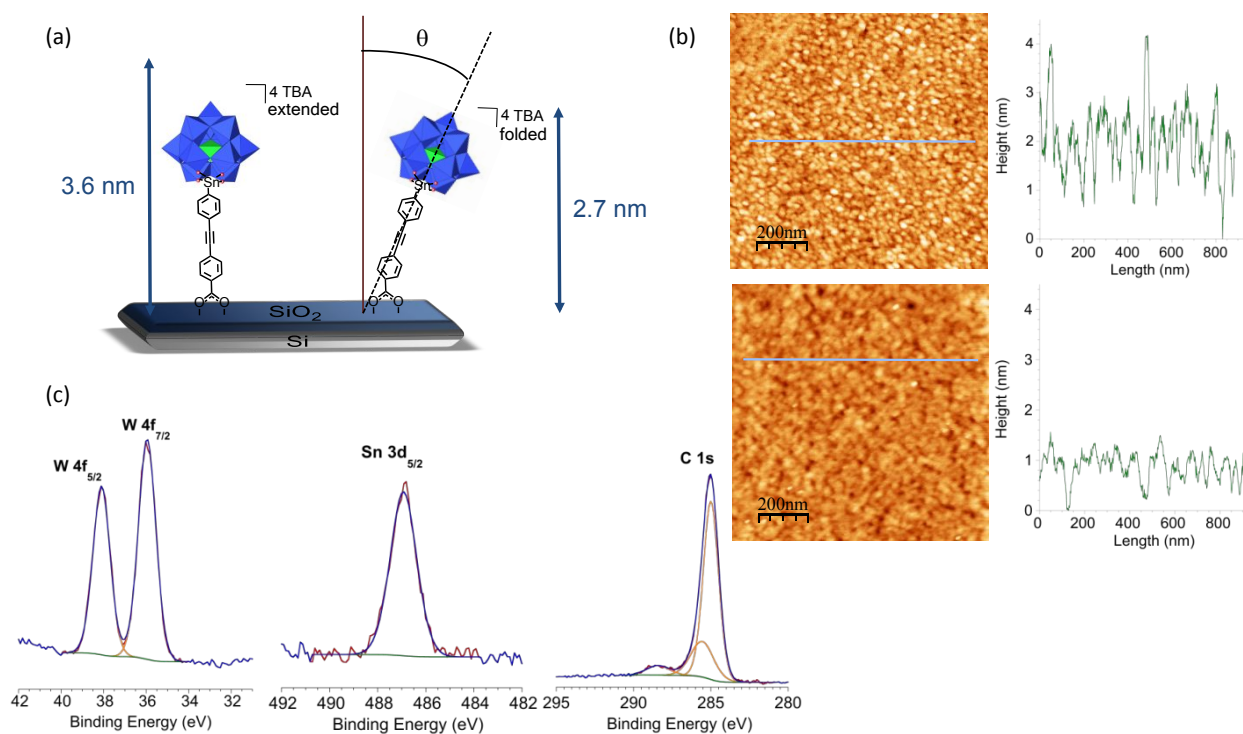


Figure 6. (a) Scheme of the extreme orientations of the $K^W_{Sn}[\text{COOH}]$ layer on Si/SiO₂ (b) 1*1 μm AFM images and z-profile of the $K^W_{Sn}[\text{COOH}]$ layer (top) compared to the freshly piranha treated Si/SiO₂ substrate (bottom) (c) W 4f, Sn 3d and C 1s high resolution XPS spectra of the $K^W_{Sn}[\text{COOH}]$ layer on Si/SiO₂.

AFM images show that the layer is rougher (RMS roughness= 0.59 nm) than the bare Si/SiO₂ substrate (RMS roughness= 0.37 nm) but still very homogeneous (figure 6b and S13), *i.e.* we do not observe large defects like holes or clusters. XPS analysis permitted to

1
2
3 detect all the POM elements on the substrate : the broad P 2p
4 photopeak, the typical W 4f_{7/2} and 4f_{5/2} doublet at 36.0 and 38.1 eV
5 respectively, and the Sn 3d_{5/2} photopeak at 486.8 eV, all these
6 values corresponding to binding energies of the elements with
7 oxygen neighbors (figure 6c and S14).⁴⁷⁻⁵⁰ Carbon and nitrogen were
8 also detected on the surface. The C 1s photopeak can be
9 deconvoluted with three contributions: the one at 285.0 eV is
10 attributed to aliphatic and aromatic C-C bonds as well as Sn-C
11 bonds, the one at 285.5 eV corresponds to the carbons linked to
12 the positively charged ammonium atom in the TBA counter-cations,
13 and the last peak at 288.4 eV, widely shifted to higher binding
14 energies, refers to the carbon linked to oxygen atoms in the
15 terminal carboxylic group (figure 6c). Only one peak appears on
16 the high-resolution spectrum of the N1s, corresponding to the
17 nitrogen of the ammonium counter-cations (figure S14).
18 Surprisingly, a significant quantity of palladium at the +2 charge
19 state is observed on the survey and the Pd high resolution spectra
20 (figure S15). The only rational explanation is to attribute this
21 impurity to the palladium-based catalyst used in the Sonogashira
22 coupling. However, XPS measurements performed on the K^W_{Sn}[COOH]
23 powder show the absence of the Pd element (on the survey spectrum
24 as well as on the high resolution spectrum performed at the Pd
25 level, figure S15). This means that palladium is present as traces
26 only in the powder but probably accumulates on the substrate.
27
28
29
30
31
32
33
34
35
36
37
38
39
40
41
42
43
44
45
46
47
48
49
50
51
52
53
54
55
56
57
58
59
60

1
2
3 Moreover, on all the other substrates we have studied until now,
4 made of similar POMs layers based on tin derivative POM hybrids
5 that had been obtained by a palladium catalyzed Sonogashira
6 coupling, but grafted on different substrates (carbon, gold,
7 hydrogenated silicon),^{33,47,51} traces of palladium had never been
8 detected. The SiO₂ layer has probably a strong affinity with
9 palladium and during the POMs deposition the palladium traces
10 accumulate on the substrate. The Pd_{5/2} photopeak at 338.0 eV
11 confirms this hypothesis as it is in accordance with Pd species in
12 an oxygenated environment.⁵² Note that in a blank sample formed
13 from the non-acidic POM K^W_{Sn}[H]), Pd²⁺ is also detected (figure S16),
14 supporting its strong interaction with SiO₂. Furthermore, the
15 proportion of Pd compared to the W element is lower (20%, compared
16 to 75% for the K^W_{Sn}[COOH] layer, see table 1), which means that the
17 carboxylic acid group is also a drainage source of the palladium
18 traces.

19
20
21
22
23
24
25
26
27
28
29
30
31
32
33
34
35
36
37
38
39 The substrate functionalized with K^W_{Si}[COOH] was also
40 characterized. The highest theoretical thickness was evaluated to
41 be at 2.6 nm with a 0.6 nm height for the organic tether, 1 nm for
42 the inorganic core of the POM and 1 nm for the extended TBA counter-
43 cations. The lowest limit for the thickness is more delicate to
44 determine theoretically as two more parameters have to be taken
45 into account: the flexibility of the tether, and the fact that the
46 POM can be attached by one or two anchoring groups (figure 7a).
47
48
49
50
51
52
53
54
55
56
57
58
59
60

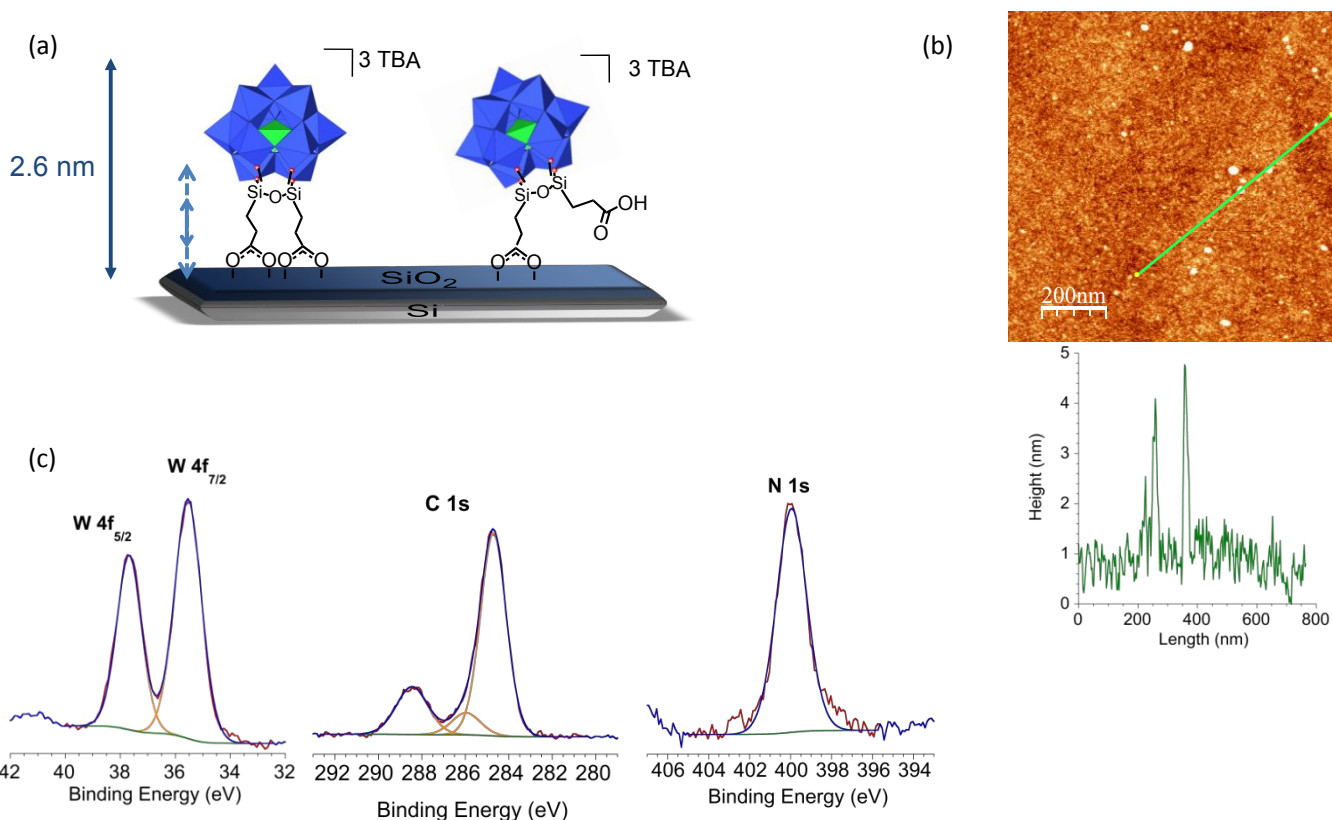


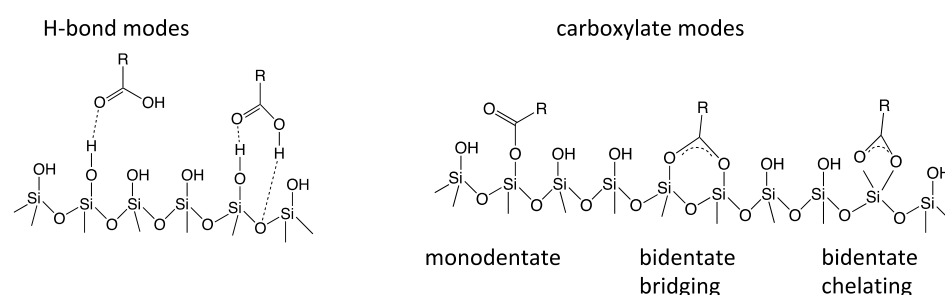
Figure 7. (a) Scheme of the possible anchoring modes of the $K_{Si}^W[COOH]$ POMs on Si/SiO₂ (b) 1*1 μm AFM image and z-profile of the $K_{Si}^W[COOH]$ layer (c) W 4f, C 1s and N 1s high resolution XPS spectra for the $K_{Si}^W[COOH]$ layer on Si/SiO₂.

On 7 samples, 6 gave satisfactory results by ellipsometry (between 1.5 and 2.5 nm, figure S12). Nevertheless, the $K_{Si}^W[COOH]$ layer is less homogeneous than the $K_{Sn}^W[COOH]$ layer, as showed by the AFM images. The layer has an overall roughness of 0.4 nm, but with some aggregates with a size around 5-8 nm are observed on the 1*1 mm image (figure 7b), and seem regularly dispersed on the surface, according to the 5*5 mm image (figure S13). The flexibility of the anchoring mode, due to the tether nature and the two carboxylic acid groups may induce more disorder in the

1
2
3 layer and explains the totally different behavior of $K_{Si}^W[COOH]$
4 compared to $K_{Sn}^W[COOH]$. XPS measurements confirmed the presence of
5 the constitutive elements of the POM (Figure 7c and S17). The high-
6 resolution spectrum in the W4f bonding energy range shows two peaks
7 at 35.5 and 37.3 eV corresponding to W4f_{7/2} and W4f_{5/2} respectively.
8 The N 1s high-resolution spectrum shows as expected a unique peak
9 at 400 eV proving the presence of the TBA counter-cations. As
10 previously, the C 1s photopeak can be deconvoluted with 3
11 contributions at 284.7, 286 and 288.5 eV corresponding
12 respectively to C-C / C-Si bonds, C-N+ bonds and C-O / C=O bonds.
13 It is worth noting that the contribution of the carbon element
14 linked to oxygen atoms is more important in the present case than
15 in the case of the $K_{Sn}^W[COOH]$ layer, in accordance with the two
16 anchoring groups present in $K_{Si}^W[COOH]$. Moreover, as expected, no
17 palladium was detected in this sample, confirming our previous
18 explanations about the origin of the Pd (Figure S17).
19
20
21
22
23
24
25
26
27
28
29
30
31
32
33
34
35
36
37
38
39
40

41 **Insights into the anchoring mode** The three surface
42 characterization techniques (AFM, XPS and ellipsometry) have thus
43 proved that we were able to build monolayers of POMs. To go
44 further, we tried to probe more specifically the SiO₂/POMs
45 interface to elucidate the grafting mode of the POMs on the SiO₂
46 layer and particularly the exact nature of the bond between the
47 carboxylic acid group and the SiO₂ layer. Indeed, various binding
48
49
50
51
52
53
54
55
56
57
58
59
60

1
2
3 modes can occur between a carboxylic acid group and an oxide
4 surface:²⁸ the bidentate carboxylate mode (chelating one silicon
5 of the surface or bridging two adjacent silicon atoms of the
6 surface), the monodentate carboxylate mode which results in the
7 formation of an ester function, and the hydrogen bond mode, in
8 which the carboxylic acid group forms H-bonds with the hydroxyl
9 groups of the surface (see figure 8).



29 **Figure 8.** Possible binding modes of carboxylic acid or carboxylate groups to silicon oxide surfaces.²⁸

30
31 Note that the rinsing step supports a covalent grafting: indeed,
32 despite a thorough rinsing, which consist in treating the POMs
33 modified substrate in a TBAPF₆ solution by an ultrasonic bath, the
34 POMs layer keeps attached, revealing a strong anchoring with the
35 substrate. To confirm this observation, a blank sample was prepared
36 by immersing a Si/SiO₂ substrate in an acetonitrile solution of
37 K^W_{sn}[H], following exactly the same procedure as for the K^W_{sn}[COOH]
38 layer. The thickness for the K^W_{sn}[H] layer measured by ellipsometry
39 after thorough rinsing is only 0.5 nm, showing that only a few
40 POMs are deposited on the surface. XPS measurements confirm this
41 observation, as the atomic percentage ratio W/Si is around 25 times
42
43
44
45
46
47
48
49
50
51
52
53
54
55
56
57
58
59
60

less important for the $K_{Sn}^W[H]$ layer than for the $K_{Sn}^W[COOH]$ layer (figure S16, Table 1).

%at	$K_{Sn}^W[COOH]$ layer	$K_{Sn}^W[H]$ layer
W	0.99	0.15
Si	13.27	49.13
Pd	0.74	0.03
W/Si	$7.4 \cdot 10^{-2}$	$3 \cdot 10^{-3}$
Pd/W	0.75	0.2

Table 1. Atomic percentages of W and Si elements in $K_{Sn}^W[COOH]$ and $K_{Sn}^W[C_6H_5]$ layers on Si/SiO₂

The $K_{Sn}^W[H]$ layer is thus constituted of a few POMs, haphazardly physisorbed and lying down on the Si/SiO₂. The carboxylic acid function is thus crucial to ensure a vertical and robust anchoring of the POMs on the substrate, which is an indirect proof that the POMs are attached via their terminal group.

To go further and try to determine the nature of the link between the POMs and the surface, FTIR measurements were performed on both carboxylic acid POMs layers, deposited on a special low-doped float-zone silicon substrate, transparent to IR radiation. To validate the technique, a drop-casting of the powders was performed on a freshly cleaned Si/SiO₂ substrate (Figure S18). In both cases, the FTIR spectrum is similar to the one registered on a KBr pellet, with the typical bands of the inorganic core of the POM below 1150 cm⁻¹ and the vibration bands characteristic of the TBA counter-cations around 2900 cm⁻¹, and at 1382, 1467 and 1485 cm⁻¹. The band corresponding to water molecules of crystallization is also

1
2
3 present in both samples, at 1675 cm^{-1} for the $\text{K}^{\text{W}}_{\text{Sn}}[\text{COOH}]$ drop-casted
4 powder and at 1656 cm^{-1} for the $\text{K}^{\text{W}}_{\text{Si}}[\text{COOH}]$ drop-casted powder. More
5 specifically on the $\text{K}^{\text{W}}_{\text{Sn}}[\text{COOH}]$ spectrum, the C=O stretching band
6 appears at 1704 cm^{-1} , and the aromatic C=C stretching band at 1606
7 cm^{-1} . The band corresponding to the asymmetric vibration of the
8 carboxylate function can be guessed at 1548 cm^{-1} . On the $\text{K}^{\text{W}}_{\text{Si}}[\text{COOH}]$
9 spectrum, the C=O stretching vibration band of the carboxylic acid
10 group is far more intense at 1710 cm^{-1} . The band at 1602 cm^{-1} can
11 be attributed to the asymmetric stretching vibration of the
12 carboxylate group, visible in this case thanks to the slight shift
13 of the band corresponding to the crystallization water molecules
14 toward 1656 cm^{-1} compared to the spectrum of the powder registered
15 in a KBr pellet.
16
17
18
19
20
21
22
23
24
25
26
27
28
29
30
31

32
33 The spectra of the POMs monolayers show different features,
34 particularly in the $1300\text{--}1700\text{ cm}^{-1}$ zone (Figure 9). On the spectrum
35 of the $\text{K}^{\text{W}}_{\text{Sn}}[\text{COOH}]$ monolayer, the C=O stretching band decreases
36 drastically relatively to two bands at 1548 and 1390 cm^{-1} that can
37 be attributed to the asymmetric and symmetric stretching mode of
38 the carboxylate function; on the spectrum of the $\text{K}^{\text{W}}_{\text{Si}}[\text{COOH}]$
39 monolayer, the C=O vibration band decreases also and two
40 carboxylate bands appear at 1570 and 1420 cm^{-1} .
41
42
43
44
45
46
47
48
49
50
51
52
53
54
55
56
57
58
59
60

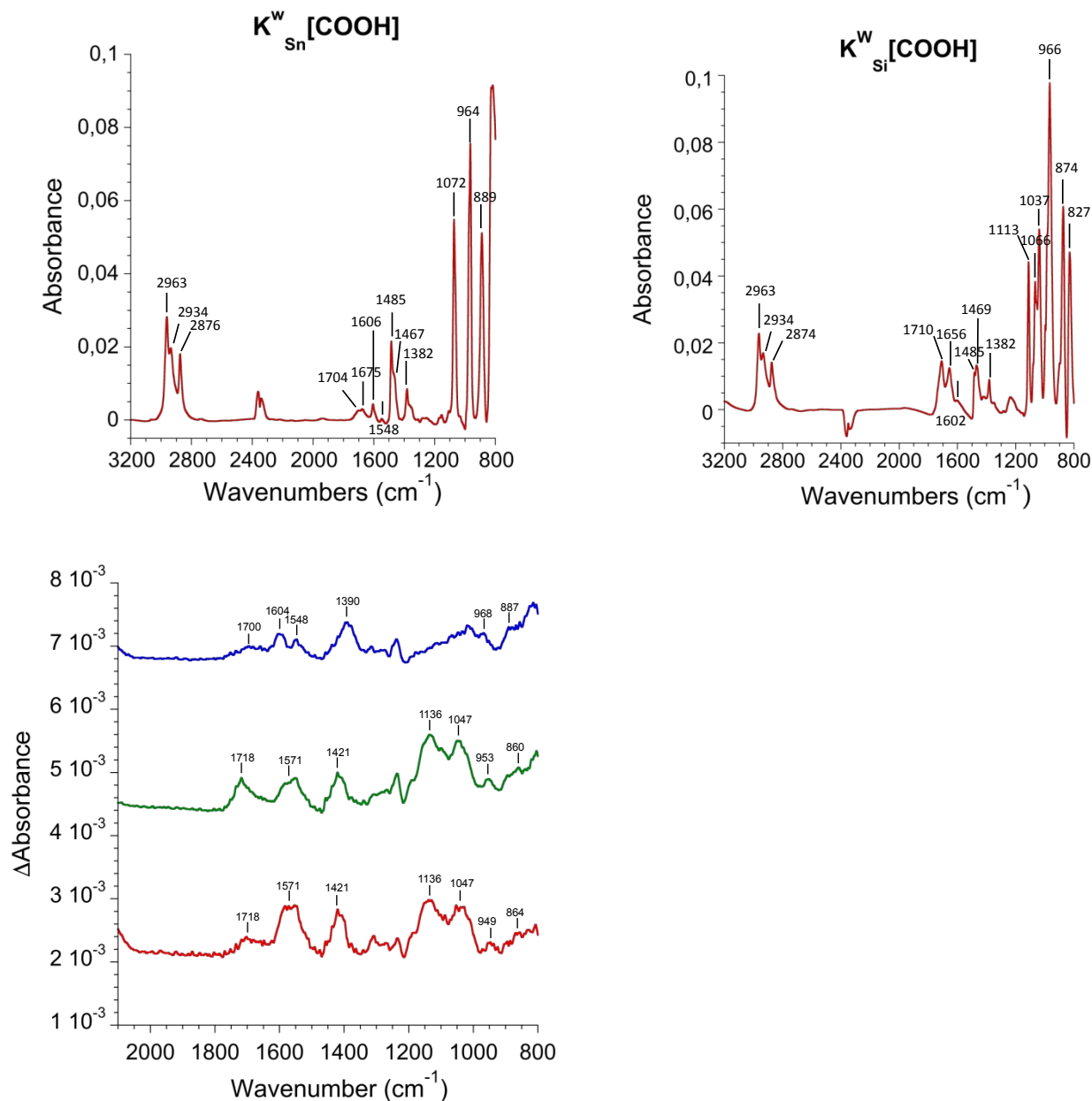


Figure 9. Top: FTIR spectra of the $K_{Sn}^W[COOH]$ (left) and $K_{Si}^W[COOH]$ (right) powders drop-casted on Si/SiO₂. Bottom: FTIR absorption spectra of the carboxylic acid POMs monolayers: $K_{Sn}^W[COOH]$ layer (blue ; $K_{Si}^W[COOH]$ layer (green ; $K_{Si}^W[COOH]$ layer (red) after an added treatment by ultrasonication. The spectra are referenced to the substrate with its cleaned thermal oxide.

As in this case the C=O was still quite intense, an additional rinsing of the surface was performed in an ultrasonic bath.

1
2
3 Interestingly, this new treatment induced a drastic decreasing of
4 the C=O band on the FTIR spectrum and no modification of the
5 carboxylate bands, showing that some additional physisorbed
6 carboxylic acid POMs were removed by an additional rinsing, but
7 that most of the POMs seem strongly attached to the surface by a
8 carboxylate group. Moreover, as usually mentioned in carboxylate
9 chemistry reports,^{53,54} the separation between the carboxylate
10 antisymmetric and symmetric stretching bands ($\Delta\nu$) can enlighten on
11 the coordination mode of the carboxylate group: $\Delta\nu=350-500\text{ cm}^{-1}$
12 corresponds to a monodentate binding to the metal atom, $\Delta\nu=150-180$
13 cm^{-1} corresponds to a bridging bidentate link to two adjacent metal
14 atoms, and $\Delta\nu=60-100\text{ cm}^{-1}$ corresponds to a chelating bidentate
15 binding mode. In the present case, the $\Delta\nu$ separation is around 150
16 cm^{-1} for both the $\text{K}_{\text{Sn}}^{\text{W}}[\text{COOH}]$ and the $\text{K}_{\text{Si}}^{\text{W}}[\text{COOH}]$ layers, which leads
17 to a bidentate binding of the carboxylate to the substrate.
18 However, discrimination between a bridging or a chelating mode is
19 more awkward with a $\Delta\nu$ value at the lower limit of the bridging
20 bidentate mode for binding to two silicon atoms of the surface. As
21 the C=O stretching band is still present, we cannot exclude that
22 several anchoring modes are present on the surface and that some
23 -COOH terminated POMs are attached via H-bonds, or that physisorbed
24 species are still present on the surface. Note that in the case of
25 the $\text{K}_{\text{Si}}^{\text{W}}[\text{COOH}]$ layer, the typical longitudinal optical (LO) and
26
27
28
29
30
31
32
33
34
35
36
37
38
39
40
41
42
43
44
45
46
47
48
49
50
51
52
53
54
55
56
57
58
59
60

transversal optical (TO) phonon modes of the silicon oxide appear at 1136 and 1047 cm^{-1} ,⁵⁵ showing that the layer of SiO_2 slightly increased during the $\text{K}_{\text{Si}}^{\text{W}}[\text{COOH}]$ deposition, probably due to the more disordered aspect of the $\text{K}_{\text{Si}}^{\text{W}}[\text{COOH}]$ monolayer, which let place to the formation of random SiO_2 islands. The characteristic bands of the POMs below 1000 cm^{-1} , typically around 960 and 870 cm^{-1} are yet detectable.

Electrical measurements

Figure 10 shows the J-V curves in a semi-log plot measured with the mercury drop technique (see experimental section) on the silicon surface without POM deposition (Si/SiO_2 reference sample cut from the same wafer), compared with $\text{K}_{\text{Sn}}^{\text{W}}[\text{COOH}]$ and $\text{K}_{\text{Si}}^{\text{W}}[\text{COOH}]$ monolayer junctions. We clearly observe three distinct families of J-V curves. Typical current density histograms at 1V are also shown and were fitted by a log-normal distribution, with a log-mean of current density $\log-\mu = -0.96$, -1.53 and -3.23 for the Si/SiO_2 reference electrode, the $\text{K}_{\text{Sn}}^{\text{W}}[\text{COOH}]$ and the $\text{K}_{\text{Si}}^{\text{W}}[\text{COOH}]$ POM junctions, respectively (*i.e.* a mean current density of 1.1×10^{-1} , 3.0×10^{-2} and 5.9×10^{-4} $\text{A}\cdot\text{cm}^{-2}$, respectively). We note that the dispersion of the current density is larger for the POMs samples than for the Si/SiO_2 sample (log standard deviations are $\log-\sigma = 0.3$, 0.54 and 0.45 for the Si/SiO_2 reference electrode, the $\text{K}_{\text{Sn}}^{\text{W}}[\text{COOH}]$ and $\text{K}_{\text{Si}}^{\text{W}}[\text{COOH}]$ POM junctions, respectively), which

may be related to the larger distribution of the POM monolayer thickness compared to the native SiO₂ (as assessed by ellipsometry and roughness AFM measurements).

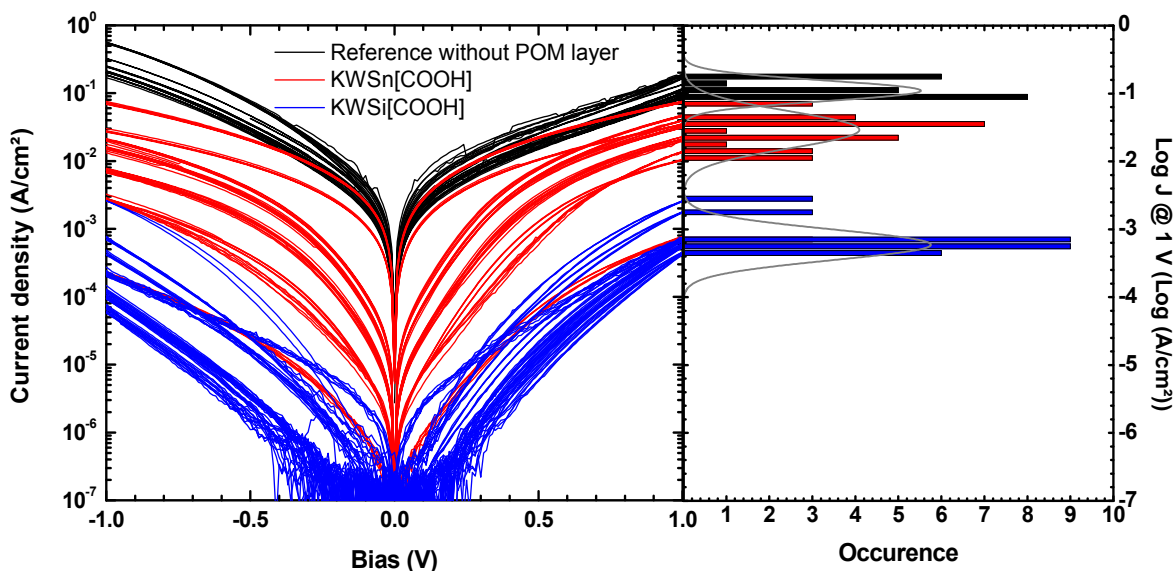


Figure 10. J-V curves measured for Si/SiO₂ reference substrate, K^W_{Sn}[COOH] and K^W_{Si}[COOH] monolayers on Si/SiO₂ (about 30 J-V curves, see details on the experimental section). Voltages were applied on the Hg drop and Si substrate was grounded.

As in previous works on similar POMs,⁵⁶ the experimental J-V curves are analyzed using an electron tunneling model. We used the so-called "modified Simmons model",⁵⁷⁻⁶¹ which introduces in the usual Simmons model for tunneling through a rectangular energy barrier⁶² a unitless adjustable non-ideality "shape factor" to take into account: (i) the deviation from the simple rectangular barrier in molecular junctions and/or a more complex barrier (here, a

1
2
3 multilayer structure composed of the silicon oxide, the organic
4 tether and the POM) (ii) a poorly defined effective mass in
5 molecular junction. The case $\alpha = 1$ corresponds to an ideal
6 rectangular barrier and a bare electron mass (reduced effective
7 electron mass=1).

$$J = \frac{e}{4\pi^2 \hbar d^2} \left\{ \left(\Phi - \frac{eV}{2} \right) \times \exp \left[-\frac{2(2m)^{1/2}}{\hbar} \alpha \left(\Phi - \frac{eV}{2} \right)^{1/2} d \right] - \left(\Phi + \frac{eV}{2} \right) \times \exp \left[-\frac{2(2m)^{1/2}}{\hbar} \alpha \left(\Phi + \frac{eV}{2} \right)^{1/2} d \right] \right\}$$

(1)

14
15
16
17
18
19
20
21
22 where J is the current density, e the electron charge, m is the
23 bare electron mass, \hbar the reduced Planck constant, d is the barrier width
24 corresponding to the thickness of the layers (native oxide, 1.4
25 nm, plus POM monolayer) measured by ellipsometry, Φ is an effective
26 barrier height, V is the applied bias and α the shape factor
27 described above.

28
29
30
31
32
33
34
35
36
37 All I-V curves (figure 10) were fitted by Eq. 1 with the two
38 parameters Φ and α (see typical fits in the supporting information,
39 Figure S19). The histograms of the effective energy barrier (Φ)
40 for the Si/SiO₂ sample, $K_{Sn}^W[\text{COOH}]$ and $K_{Si}^W[\text{COOH}]$ junctions are given
41 in Figure 11 and fitted by a Gaussian law. We observe a clear
42 offset towards higher values for the $K_{Sn}^W[\text{COOH}]$ compared to the
43 $K_{Si}^W[\text{COOH}]$, with mean values of $\Phi = 1.75$ eV (standard deviation 0.12
44 eV) and $\Phi = 1.39$ eV (standard deviation 0.23 eV), respectively.
45
46
47
48
49
50
51
52
53
54
55
56 For the reference sample, we have $\Phi = 1.91$ eV (standard deviation

0.13 eV), which is consistent with previous values for native SiO₂.⁶³ We note that it seems counterintuitive to observe a higher current (figure 10) for the sample K^W_{sn}[COOH] with a higher energy barrier (figure 11) and the thicker monolayer (see figures 2 and 3). This feature is understood if we consider the smaller values of the shape factor α (0.26-0.43) for this K^W_{sn}[COOH] sample compared to $\alpha = 0.69-0.87$ for the K^W_{si}[COOH] sample (see supporting information Figure S20). In Eq. 1 the dominant term is $\exp(-\alpha\Phi^{1/2}d)$ and we have a smaller average value $\alpha\Phi^{1/2}d \approx 2.3$ for the K^W_{sn}[COOH] sample than $\alpha\Phi^{1/2}d \approx 3.1$ for the K^W_{si}[COOH] sample, thus consistent with a higher current for the former one (with average thicknesses $d=5.1$ nm and 3.3 nm, respectively, i.e. 1.4 nm for the native oxide plus the POM layer thickness, see ellipsometry results). We suggest that this difference of the shape factor is likely related to the nature of the organic tether of the POM hybrid, π -conjugated vs. σ -saturated. It is known that the exact potential distribution in a molecular junction is more complicated in a π -conjugated moiety, while it is more linear through alkyl chains (see a typical example in reference 62),⁶⁴ which is consistent with a shape factor closer to ideality in this latter case. Note also that we cannot exclude an additional effect of the Pd²⁺ cations present in the K^W_{sn}[COOH] layers on the intensity of the observed current.

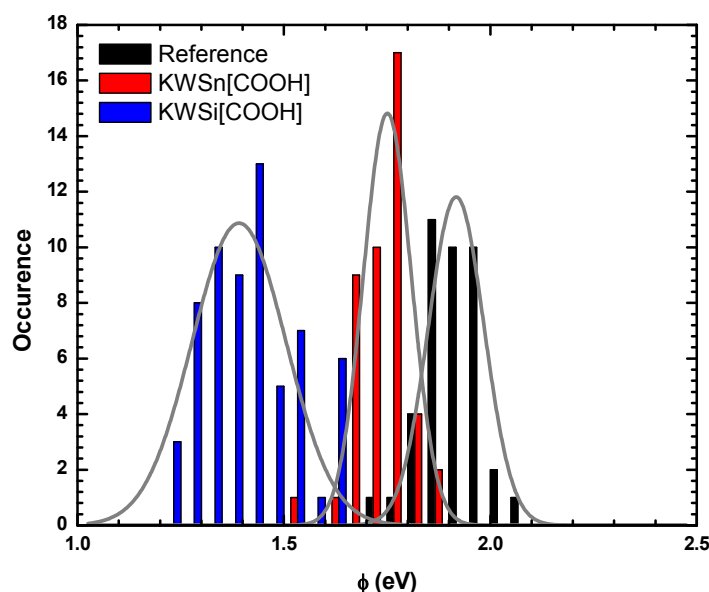


Figure 11. Effective barrier height Φ histograms for $K^{W}_{Sn}[COOH]$, $K^{W}_{Si}[COOH]$ monolayers and the reference bare Si/SiO₂ sample.

We can further refine the electronic structure analysis of the Si/SiO₂/POM junctions. The effective energy barrier is made of two parts, the native SiO₂ ($\Phi \approx 1.9$ eV, $d \approx 1.4$ nm) and the POM monolayer characterized by the energy position of the POM LUMO, ϵ_{POM} , with respect to the Fermi energy of the electrodes. We ascribe the molecular orbital involved in the electron transport to the LUMO of the POMs, which are the closest to the Fermi energy of electrodes (see DFT calculations) while the HOMOs are deeper in energy. The lower Φ for the two POM samples means that the LUMO is lower in energy. Assuming a simple staircase energy barrier model (Figure 12, details in the supporting information and reference

63),⁶⁵ we can deduce the energy position of the POM LUMO, ϵ_{POM} at 1.1 eV and 1.7 eV for the $\text{K}_{\text{Si}}^{\text{W}}[\text{COOH}]$ and $\text{K}_{\text{Sn}}^{\text{W}}[\text{COOH}]$ samples, respectively. Finally, we compare these LUMO energy positions, with the ones determined from cyclic voltammograms and DFT calculations (Figure 12). The LUMO positions from CV in solution and the DFT calculations (continuum solvation model) are in good quantitative agreement, and in good qualitative agreement with the values from the electrical measurements on the "solid-state" molecular device (LUMO of $\text{K}_{\text{Si}}^{\text{W}}[\text{COOH}]$ lower than $\text{K}_{\text{Sn}}^{\text{W}}[\text{COOH}]$). The LUMO energy differences are consistent for the three methods (0.6 eV). The fact that the LUMOs are shifted in the molecular junctions may be due to molecule/electrode coupling and charge transfer and/or the presence of trapped charges in the native SiO_2 layer. In solution, solvation is also expected to stabilize the energy levels.

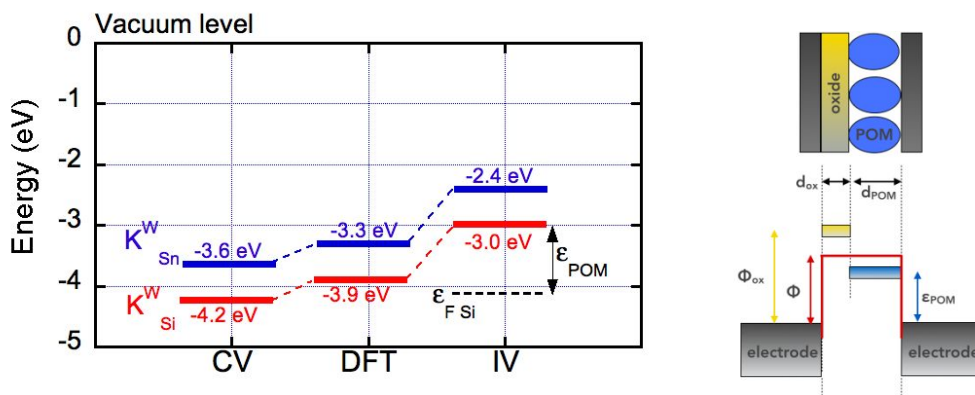


Figure 12. LUMO energy positions with respect to the vacuum level. The DFT position is given by the first empty d orbital of the POMs (see "DFT section").

1
2
3 The CV position is calculated from the first reduction waves (Figure S10),
4
5 $E_{\text{LUMO}} = -(E_{1/2} + E_{\text{SCE/SHE}}) - 4.4$ (in eV with $E_{\text{SCE/SHE}} = 0.24$ eV).⁶⁶ The IV position is obtained
6
7 from the ϵ_{POM} value considering the n^+ doped silicon Fermi energy at -4.1 eV (Si
8 electron affinity) and the junction energy diagram shown in the right (see
9 details in the Supporting Information and in a previous publication⁶⁵).

10
11
12
13
14
15 Finally, we note that the LUMO position of the $K_{\text{Sn}}^{\text{W}}[\text{COOH}]$ POM is
16
17 consistent with the position of similar molecule $K_{\text{Sn}}^{\text{W}}[\text{N}_2^+]$ grafted
18
19 on hydrogen-terminated silicon (no oxide) using a diazonium group
20
21 instead of a carboxylic acid one ($\epsilon_{\text{POM}} = 1.8$ eV in reference 53 vs.
22
23 1.7 eV here),⁵⁶ which indicates that the electronic structure of
24
25 these molecular junctions is mainly controlled by the POM LUMO. As
26
27 noted above the LUMOs of the POM hybrids are combination of
28
29 tungsten d orbitals and do not involve the orbitals of the tether
30
31 or the anchor group. The shifting down of about 0.6 eV on going
32
33 from $K_{\text{Sn}}^{\text{W}}[\text{COOH}]$ to $K_{\text{Si}}^{\text{W}}[\text{COOH}]$ (molecule in solution, in a solvation
34
35 continuum model, as well as for the "solid-state" self-assembled
36
37 monolayers) is rather attributable to the change in the total
38
39 charge (4- for $K_{\text{Sn}}^{\text{W}}[\text{COOH}]$ vs 3- for $K_{\text{Si}}^{\text{W}}[\text{COOH}]$).⁶⁷

40 41 42 43 44 45 46 CONCLUSION

47
48
49 Two POM hybrids $\text{TBA}_{4.4}[\text{PW}_{11}\text{O}_{39}\{\text{Sn}(\text{C}_6\text{H}_4)\text{C}\equiv\text{C}(\text{C}_6\text{H}_4)\text{COOH}_{0.6}\}]$ ($K_{\text{Sn}}^{\text{W}}[\text{COOH}]$)
50
51 and $\text{TBA}_{3.4}[\text{PW}_{11}\text{O}_{39}\{\text{O}(\text{SiC}_2\text{H}_4\text{COOH}_{0.8})_2\}]$ ($K_{\text{Si}}^{\text{W}}[\text{COOH}]$) have been prepared
52
53 and thoroughly characterized in solution by NMR, UV-visible
54
55 spectroscopies and cyclic-voltammetry. They display remote
56
57
58
59
60

1
2
3 carboxylic acid/carboxylate groups that allow investigating their
4 covalent grafting onto Si/SiO₂ flat substrates. Monolayers have
5 been obtained and characterized by ellipsometry, AFM, and XPS. The
6 K^W_{Si}[COOH] layer was found to be less uniform than the K^W_{Sn}[COOH]
7 layer, presumably because of the presence of two, moreover more
8 flexible, aliphatic arms. An FTIR study was carried out on a
9 special low doped float-zone silicon substrate to probe the POM
10 binding mode, from which a bidentate carboxylate was inferred.
11 Finally, the electronic properties of the POM hybrids disclosed by
12 cyclic-voltammetry, electronic absorption spectroscopy and
13 calculated energy level diagrams have been confronted to the
14 energetics of the Si/SiO₂//POM layer//Hg junction as probed by
15 electron transport measurements at the solid state.

16
17 These three approaches are consistent, showing that the energy
18 position of the LUMO of K^W_{Si}[COOH] is lower than the one of K^W_{Sn}[COOH]
19 by a difference of 0.6 eV, in agreement with a higher total charge
20 for the later. The LUMO energy of K^W_{Sn}[COOH] grafted on Si/SiO₂ and
21 of K^W_{Sn}[N₂⁺] grafted on silicon (no oxide) are similar, showing that
22 the electronic properties of these molecular junctions are driven
23 by the POM LUMO (d-orbitals) and not by the π-orbitals of the
24 tether or the anchor group. Such POM-based electrodes represent
25 new functionalized silicon-based electrodes, which have important
26 implications for improving and/or tuning the electronic properties
27 of a variety of electronic devices: photovoltaics, sensors,
28
29
30
31
32
33
34
35
36
37
38
39
40
41
42
43
44
45
46
47
48
49
50
51
52
53
54
55
56
57
58
59
60

1
2
3 memories and bioelectronics.⁶⁸ Some of us have recently shown that
4
5 the controlled grafting of POMs on various oxides is also relevant
6
7 to energy conversion.⁶⁹
8
9
10
11
12
13

14 ASSOCIATED CONTENT

15
16
17 **Supporting Information** file includes: ¹H and ³¹P NMR spectra of
18
19 $K_{Sn}^W[COOH]$ and $K_{Si}^W[COOH]$; Infrared spectrum of $K_{Sn}^W[COOH]$ and
20
21 $K_{Si}^W[COOH]$ in KBr pellets; ESI⁻ spectra of 1 $\mu\text{mol}\cdot\text{L}^{-1}$ of $K_{Sn}^W[COOH]$
22
23 and $K_{Si}^W[COOH]$ in acetonitrile ; cyclic voltammograms of $K_{Sn}^W[COOH]$
24
25 in acetonitrile; thickness histograms inferred from ellipsometry;
26
27 AFM images of the $K_{Sn}^W[COOH]$ and $K_{Si}^W[COOH]$ layers; XPS
28
29 characterization; FTIR spectra of the $K_{Sn}^W[COOH]$ and $K_{Si}^W[COOH]$
30
31 powders drop-casted on Si/SiO₂; example of fits of IV curves using
32
33 the modified Simmons model; description of the two layers staircase
34
35 energy model; XYZ coordinates from the DFT calculation. The file
36
37 is available free of charge as a PDF file.
38
39
40
41
42
43
44
45
46
47
48

49 AUTHOR INFORMATION

50 51 **Corresponding Author**

52
53
54
55
56
57
58
59
60

1
2
3 **Anna Proust** - Sorbonne Université, CNRS, Institut Parisien de
4 Chimie Moléculaire, IPCM, 4 Place Jussieu, F-75005 Paris, France;
5
6
7 orcid.org/0000-0002-0903-6507;
8
9

10 Email : anna.proust@sorbonne-universite.fr
11
12
13

14 **Authors**

15
16

17 **Maxime Laurans, Kelly Trinh, Kevin Dalla Francesca, Guillaume**
18 **Izzet, Sandra Alves, Etienne Derat, Florence Volatron** - Sorbonne
19 Université, CNRS, Institut Parisien de Chimie Moléculaire, IPCM,
20 4 Place Jussieu, F-75005 Paris, France
21
22
23
24
25
26
27

28 **Kelly Trinh, Olivier Pluchery** - Sorbonne Université, CNRS,
29 Institut des Nanosciences de Paris, INSP, 4 Place Jussieu, F-75005
30 Paris, France
31
32
33
34
35

36 **Dominique Vuillaume, Stéphane Lenfant** - Institute for Electronics
37 Microelectronics and Nanotechnology (IEMN), CNRS, Av. Poincaré,
38 Villeneuve d'Ascq, France
39
40
41
42
43

44 **Vincent Humblot** - Sorbonne Université, CNRS, Laboratoire de
45 réactivité de surface, LRS, 4 Place Jussieu, F-75005 Paris, France-
46
47 present address : FEMTO-ST Institute, UMR CNRS 6174, Université Bourgogne
48 Franche-Comté, 15B avenue des Montboucons, 25030 Besançon Cedex, France
49
50
51
52
53
54
55
56
57
58
59
60

Author Contributions

The manuscript was written through contributions of all authors. All authors have given approval to the final version of the manuscript.

Funding Sources

This work was supported by Sorbonne Université and by the CNRS. K.D.F. thanks the program PER-SU of Sorbonne Universités for his post-doctoral grant.

ACKNOWLEDGMENT

The authors acknowledge IMPC from Sorbonne University (Institut des Matériaux de Paris Centre, FR CNRS 2482) and the C'Nano projects of the Region Ile-de-France, for Omicron XPS apparatus funding. KT is grateful to Youssef Ben B'Marek for his advice for the synthesis of $K_{Sn}^W[COOH]$ and Raphaël Salles for his help in drawing Figure S10.

ABBREVIATIONS

POM, polyoxometalate; AFM, atomic force microscopy; XPS, X-ray photoelectron spectroscopy; FTIR, Fourier Transform Infra Red.

REFERENCES

- (1) Busche, C.; Vilà-Nadal, L.; Yan, J.; Miras, H. N.; Long, D.-L.; Georgiev, V. P.; Asenov, A.; Pedersen, R. H.; Gadegaard, N.; Mirza, M. M.; Paul, D. J.; Poblet, J. M.; Cronin, L. Design and Fabrication of Memory Devices Based on Nanoscale Polyoxometalate Clusters. *Nature* **2014**, *515* (7528), 545–549. <https://doi.org/10.1038/nature13951>.
- (2) Chen, X.; Huang, P.; Zhu, X.; Zhuang, S.; Zhu, H.; Fu, J.; Nissimagoudar, A. S.; Li, W.;

Zhang, X.; Zhou, L.; Wang, Y.; Lv, Z.; Zhou, Y.; Han, S.-T. Keggin-Type Polyoxometalate Cluster as an Active Component for Redox-Based Nonvolatile Memory. *Nanoscale Horizons* **2019**, *4* (3), 697–704. <https://doi.org/10.1039/C8NH00366A>.

(3) Walsh, J. J.; Bond, A. M.; Forster, R. J.; Keyes, T. E. Hybrid Polyoxometalate Materials for Photo(Electro-) Chemical Applications. *Coordination Chemistry Reviews* **2016**, *306*, 217–234. <https://doi.org/10.1016/j.ccr.2015.06.016>.

(4) Miras, H. N.; Yan, J.; Long, D.-L.; Cronin, L. Engineering Polyoxometalates with Emergent Properties. *Chemical Society Reviews* **2012**, *41* (22), 7403. <https://doi.org/10.1039/c2cs35190k>.

(5) Ji, Y.; Huang, L.; Hu, J.; Streb, C.; Song, Y.-F. Polyoxometalate-Functionalized Nanocarbon Materials for Energy Conversion, Energy Storage and Sensor Systems. *Energy & Environmental Science* **2015**, *8* (3), 776–789. <https://doi.org/10.1039/C4EE03749A>.

(6) VanGelder, L. E.; Kosswattaarachchi, A. M.; Forrestel, P. L.; Cook, T. R.; Matson, E. M. Polyoxovanadate-Alkoxide Clusters as Multi-Electron Charge Carriers for Symmetric Non-Aqueous Redox Flow Batteries. *Chem. Sci.* **2018**, *9* (6), 1692–1699. <https://doi.org/10.1039/C7SC05295B>.

(7) Friedl, J.; Holland-Cunz, M. V.; Cording, F.; Pfanschilling, F. L.; Wills, C.; McFarlane, W.; Schrickler, B.; Fleck, R.; Wolfschmidt, H.; Stimming, U. Asymmetric Polyoxometalate Electrolytes for Advanced Redox Flow Batteries. *Energy Environ. Sci.* **2018**, *11* (10), 3010–3018. <https://doi.org/10.1039/C8EE00422F>.

(8) Chen, L.; Chen, W.-L.; Wang, X.-L.; Li, Y.-G.; Su, Z.-M.; Wang, E.-B. Polyoxometalates in Dye-Sensitized Solar Cells. *Chem. Soc. Rev.* **2019**, *48* (1), 260–284. <https://doi.org/10.1039/C8CS00559A>.

(9) Liu, R.; Zhang, G.; Cao, H.; Zhang, S.; Xie, Y.; Haider, A.; Kortz, U.; Chen, B.; Dalal, N. S.; Zhao, Y.; Zhi, L.; Wu, C.-X.; Yan, L.-K.; Su, Z.; Keita, B. Enhanced Proton and Electron Reservoir Abilities of Polyoxometalate Grafted on Graphene for High-Performance Hydrogen Evolution. *Energy Environ. Sci.* **2016**, *9* (3), 1012–1023. <https://doi.org/10.1039/C5EE03503A>.

(10) Zhu, H.; Pookpanratana, S. J.; Bonevich, J. E.; Natoli, S. N.; Hacker, C. A.; Ren, T.; Suehle, J. S.; Richter, C. A.; Li, Q. Redox-Active Molecular Nanowire Flash Memory for High-Endurance and High-Density Nonvolatile Memory Applications. *ACS Applied Materials & Interfaces* **2015**, *7* (49), 27306–27313. <https://doi.org/10.1021/acsami.5b08517>.

(11) Balliou, A.; Douvas, A. M.; Normand, P.; Tsikritzis, D.; Kennou, S.; Argitis, P.; Glezos, N. Tungsten Polyoxometalate Molecules as Active Nodes for Dynamic Carrier Exchange in Hybrid Molecular/Semiconductor Capacitors. *Journal of Applied Physics* **2014**, *116* (14), 143703. <https://doi.org/10.1063/1.4897397>.

(12) Li, J.-S.; Sang, X.-J.; Chen, W.-L.; Zhang, L.-C.; Zhu, Z.-M.; Ma, T.-Y.; Su, Z.-M.; Wang, E.-B. Enhanced Visible Photovoltaic Response of TiO₂ Thin Film with an All-Inorganic Donor–Acceptor Type Polyoxometalate. *ACS Applied Materials & Interfaces* **2015**, *7* (24), 13714–13721. <https://doi.org/10.1021/acsami.5b03948>.

- 1
2
3 (13) El Moll, H.; Black, F. A.; Wood, C. J.; Al-Yasari, A.; Reddy Marri, A.; Sazanovich, I. V.;
4 Gibson, E. A.; Fielden, J. Increasing P-Type Dye Sensitised Solar Cell Photovoltages Using
5 Polyoxometalates. *Physical Chemistry Chemical Physics* **2017**, *19* (29), 18831–18835.
6 <https://doi.org/10.1039/C7CP01558E>.
7
8
9 (14) Xiang, X.; Fielden, J.; Rodríguez-Córdoba, W.; Huang, Z.; Zhang, N.; Luo, Z.; Musaev,
10 D. G.; Lian, T.; Hill, C. L. Electron Transfer Dynamics in Semiconductor–Chromophore–
11 Polyoxometalate Catalyst Photoanodes. *The Journal of Physical Chemistry C* **2013**, *117* (2), 918–
12 926. <https://doi.org/10.1021/jp312092u>.
13
14 (15) Alaaeddine, M.; Zhu, Q.; Fichou, D.; Izzet, G.; Rault, J. E.; Barrett, N.; Proust, A.; Tortech,
15 L. Enhancement of Photovoltaic Efficiency by Insertion of a Polyoxometalate Layer at the Anode
16 of an Organic Solar Cell. *Inorg. Chem. Front.* **2014**, *1* (9), 682–688.
17 <https://doi.org/10.1039/C4QI00093E>.
18
19 (16) Bae, S.; Kim, H.; Jeon, D.; Ryu, J. Catalytic Multilayers for Efficient Solar Water
20 Oxidation through Catalyst Loading and Surface-State Passivation of BiVO₄ Photoanodes. *ACS*
21 *Applied Materials & Interfaces* **2019**, *11* (8), 7990–7999. <https://doi.org/10.1021/acsami.8b20785>.
22
23 (17) Fielden, J.; Sumliner, J. M.; Han, N.; Geletii, Y. V.; Xiang, X.; Musaev, D. G.; Lian, T.;
24 Hill, C. L. Water Splitting with Polyoxometalate-Treated Photoanodes: Enhancing Performance
25 through Sensitizer Design. *Chemical Science* **2015**, *6* (10), 5531–5543.
26 <https://doi.org/10.1039/C5SC01439E>.
27
28 (18) Lauinger, S. M.; Sumliner, J. M.; Yin, Q.; Xu, Z.; Liang, G.; Glass, E. N.; Lian, T.; Hill,
29 C. L. High Stability of Immobilized Polyoxometalates on TiO₂ Nanoparticles and Nanoporous
30 Films for Robust, Light-Induced Water Oxidation. *Chemistry of Materials* **2015**, *27* (17), 5886–
31 5891. <https://doi.org/10.1021/acs.chemmater.5b01248>.
32
33 (19) Lauinger, S. M.; Piercy, B. D.; Li, W.; Yin, Q.; Collins-Wildman, D. L.; Glass, E. N.;
34 Losego, M. D.; Wang, D.; Geletii, Y. V.; Hill, C. L. Stabilization of Polyoxometalate Water
35 Oxidation Catalysts on Hematite by Atomic Layer Deposition. *ACS Applied Materials &*
36 *Interfaces* **2017**, *9* (40), 35048–35056. <https://doi.org/10.1021/acsami.7b12168>.
37
38 (20) Zheng, X.; Chen, W.; Chen, L.; Wang, Y.; Guo, X.; Wang, J.; Wang, E. A Strategy for
39 Breaking Polyoxometalate-Based MOFs To Obtain High Loading Amounts of Nanosized
40 Polyoxometalate Clusters to Improve the Performance of Dye-Sensitized Solar Cells. *Chemistry -*
41 *A European Journal* **2017**, *23* (37), 8871–8878. <https://doi.org/10.1002/chem.201701103>.
42
43 (21) Sang, X.; Li, J.; Zhang, L.; Wang, Z.; Chen, W.; Zhu, Z.; Su, Z.; Wang, E. A Novel
44 Carboxyethyltin Functionalized Sandwich-Type Germanotungstate: Synthesis, Crystal Structure,
45 Photosensitivity, and Application in Dye-Sensitized Solar Cells. *ACS Applied Materials &*
46 *Interfaces* **2014**, *6* (10), 7876–7884. <https://doi.org/10.1021/am501192f>.
47
48 (22) Raula, M.; Gan Or, G.; Saganovich, M.; Zeiri, O.; Wang, Y.; Chierotti, M. R.; Gobetto, R.;
49 Weinstock, I. A. Polyoxometalate Complexes of Anatase-Titanium Dioxide Cores in Water.
50 *Angewandte Chemie International Edition* **2015**, *54* (42), 12416–12421.
51 <https://doi.org/10.1002/anie.201501941>.
52
53
54
55
56
57
58
59
60

- 1
2
3 (23) Chakraborty, B.; Gan-Or, G.; Raula, M.; Gadot, E.; Weinstock, I. A. Design of an
4 Inherently-Stable Water Oxidation Catalyst. *Nat Commun* **2018**, *9* (1), 4896.
5 <https://doi.org/10.1038/s41467-018-07281-z>.
6
- 7 (24) Villanneau, R.; Marzouk, A.; Wang, Y.; Djamaa, A. B.; Laugel, G.; Proust, A.; Launay, F.
8 Covalent Grafting of Organic–Inorganic Polyoxometalates Hybrids onto Mesoporous SBA-15: A
9 Key Step for New Anchored Homogeneous Catalysts. *Inorganic Chemistry* **2013**, *52* (6), 2958–
10 2965. <https://doi.org/10.1021/ic302374v>.
11
- 12 (25) Tountas, M.; Topal, Y.; Verykios, A.; Soultati, A.; Kaltzoglou, A.; Papadopoulos, T. A.;
13 Auras, F.; Seintis, K.; Fakis, M.; Palilis, L. C.; Tsikritzis, D.; Kennou, S.; Fakharuddin, A.;
14 Schmidt-Mende, L.; Gardelis, S.; Kus, M.; Falaras, P.; Davazoglou, D.; Argitis, P.; Vasilopoulou,
15 M. A Silanol-Functionalized Polyoxometalate with Excellent Electron Transfer Mediating
16 Behavior to ZnO and TiO₂ Cathode Interlayers for Highly Efficient and Extremely Stable Polymer
17 Solar Cells. *Journal of Materials Chemistry C* **2018**, *6* (6), 1459–1469.
18 <https://doi.org/10.1039/C7TC04960A>.
19
- 20 (26) García-López, V.; Palacios-Corella, M.; Clemente-León, M.; Coronado, E. Iron(II)
21 Complex of 2-(1H-Pyrazol-1-Yl)Pyridine-4-Carboxylic Acid (PpCOOH) Suitable for Surface
22 Deposition. *Journal of Coordination Chemistry* **2018**, *71* (6), 763–775.
23 <https://doi.org/10.1080/00958972.2018.1430790>.
24
- 25 (27) Murata, H.; Baskett, M.; Nishide, H.; Lahti, P. M. Adsorption of a Carboxylic Acid-
26 Functionalized Aminoxyl Radical onto SiO₂. *Langmuir* **2014**, *30* (14), 4026–4032.
27 <https://doi.org/10.1021/la5000952>.
28
- 29 (28) Pujari, S. P.; Scheres, L.; Marcelis, A. T. M.; Zuilhof, H. Covalent Surface Modification
30 of Oxide Surfaces. *Angewandte Chemie International Edition* **2014**, *53* (25), 6322–6356.
31 <https://doi.org/10.1002/anie.201306709>.
32
- 33 (29) Ichimura, K.; Funabiki, A.; Aoki, K.; Akiyama, H. Solid Phase Adsorption of Crystal
34 Violet Lactone on Silica Nanoparticles to Probe Mechanochemical Surface Modification.
35 *Langmuir* **2008**, *24* (13), 6470–6479. <https://doi.org/10.1021/la8002178>.
36
- 37 (30) Du, Y.; Du, Z.; Zou, W.; Li, H.; Mi, J.; Zhang, C. Carbon Dioxide Adsorbent Based on
38 Rich Amines Loaded Nano-Silica. *Journal of Colloid and Interface Science* **2013**, *409*, 123–128.
39 <https://doi.org/10.1016/j.jcis.2013.07.071>.
40
- 41 (31) Matt, B.; Moussa, J.; Chamoreau, L.-M.; Afonso, C.; Proust, A.; Amouri, H.; Izzet, G.
42 Elegant Approach to the Synthesis of a Unique Heteroleptic Cyclometalated Iridium(III)-
43 Polyoxometalate Conjugate. *Organometallics* **2012**, *31* (1), 35–38.
44 <https://doi.org/10.1021/om200910p>.
45
- 46 (32) Souchay, P. *Polyanions and Polycations*; Gauthier-Villars:Paris, 1963.
47
- 48 (33) Gam Derouich, S.; Rinfray, C.; Izzet, G.; Pinson, J.; Gallet, J.-J.; Kanoufi, F.; Proust, A.;
49 Combellas, C. Control of the Grafting of Hybrid Polyoxometalates on Metal and Carbon Surfaces:
50 Toward Submonolayers. *Langmuir* **2014**, *30* (8), 2287–2296. <https://doi.org/10.1021/la500067e>.
51
52
53
54
55
56
57
58
59
60

- 1
2
3 (34) Zeghbroek, B. V. Principle of Conductor Devices.
4
- 5 (35) Izzet, G.; Volatron, F.; Proust, A. Tailor-Made Covalent Organic-Inorganic
6 Polyoxometalate Hybrids: Versatile Platforms for the Elaboration of Functional Molecular
7 Architectures. *The Chemical Record* **2017**, *17* (2), 250–266.
8 <https://doi.org/10.1002/tcr.201600092>.
9
- 10 (36) Elgrishi, N.; Chambers, M. B.; Wang, X.; Fontecave, M. Molecular Polypyridine-Based
11 Metal Complexes as Catalysts for the Reduction of CO₂. *Chem. Soc. Rev.* **2017**, *46* (3), 761–796.
12 <https://doi.org/10.1039/C5CS00391A>.
13
- 14 (37) Rinfray, C.; Renaudineau, S.; Izzet, G.; Proust, A. A Covalent Polyoxomolybdate-Based
15 Hybrid with Remarkable Electron Reservoir Properties. *Chem. Commun.* **2014**, *50* (62), 8575–
16 8577. <https://doi.org/10.1039/C4CC03779K>.
17
- 18 (38) Rinfray, C.; Brasiliense, V.; Izzet, G.; Volatron, F.; Alves, S.; Combellas, C.; Kanoufi, F.;
19 Proust, A. Electron Transfer to a Phosphomolybdate Monolayer on Glassy Carbon: Ambivalent
20 Effect of Protonation. *Inorganic Chemistry* **2016**, *55* (14), 6929–6937.
21 <https://doi.org/10.1021/acs.inorgchem.6b00485>.
22
- 23 (39) Matt, B.; Renaudineau, S.; Chamoreau, L.-M.; Afonso, C.; Izzet, G.; Proust, A. Hybrid
24 Polyoxometalates: Keggin and Dawson Silyl Derivatives as Versatile Platforms. *The Journal of*
25 *Organic Chemistry* **2011**, *76* (9), 3107–3112. <https://doi.org/10.1021/jo102546v>.
26
- 27 (40) Duffort, V.; Thouvenot, R.; Afonso, C.; Izzet, G.; Proust, A. Straightforward Synthesis of
28 New Polyoxometalate-Based Hybrids Exemplified by the Covalent Bonding of a Polypyridyl
29 Ligand. *Chemical Communications* **2009**, No. 40, 6062. <https://doi.org/10.1039/b913475a>.
30
- 31 (41) Furche, F.; Ahlrichs, R.; Hättig, C.; Klopper, W.; Sierka, M.; Weigend, F. Turbomole.
32 *WIREs Comput Mol Sci* **2014**, *4* (2), 91–100. <https://doi.org/10.1002/wcms.1162>.
33
- 34 (42) Dwyer, A. D.; Tozer, D. J. Effect of Chemical Change on TDDFT Accuracy: Orbital
35 Overlap Perspective of the Hydrogenation of Retinal. *Phys. Chem. Chem. Phys.* **2010**, *12* (12),
36 2816. <https://doi.org/10.1039/c002428g>.
37
- 38 (43) Ahmed, I.; Farha, R.; Goldmann, M.; Ruhlmann, L. A Molecular Photovoltaic System
39 Based on Dawson Type Polyoxometalate and Porphyrin Formed by Layer-by-Layer Self
40 Assembly. *Chem. Commun.* **2013**, *49* (5), 496–498. <https://doi.org/10.1039/C2CC37519B>.
41
- 42 (44) Yang, Y.; Xu, L.; Li, F.; Du, X.; Sun, Z. Enhanced Photovoltaic Response by Incorporating
43 Polyoxometalate into a Phthalocyanine-Sensitized Electrode. *Journal of Materials Chemistry*
44 **2010**, *20* (48), 10835. <https://doi.org/10.1039/c0jm01812k>.
45
- 46 (45) Siddarth, A. S.; Miao, W. Photoelectrochemical Studies on Earth Abundant Pentanickel
47 Polyoxometalates as Co-Catalysts for Solar Water Oxidation. *Sustainable Energy & Fuels* **2018**,
48 *2* (4), 827–835. <https://doi.org/10.1039/C7SE00523G>.
49
- 50 (46) Ye, H.-Y.; Qi, J.-M.; Sun, R.; Gao, L.-H.; Wang, K.-Z. Photoelectric Active Hybrid Film
51 Based on RuII Terpyridyl Complex and EuIII Substituted Keggin Polyoxometalate of
52 [Eu(BW11O39)2]15-. *Electrochimica Acta* **2017**, *256*, 291–298.
53
54
55
56
57
58
59
60

1
2
3 <https://doi.org/10.1016/j.electacta.2017.10.028>.

4
5 (47) Volatron, F.; Noël, J.-M.; Rinfray, C.; Decorse, P.; Combellas, C.; Kanoufi, F.; Proust, A.
6 Electron Transfer Properties of a Monolayer of Hybrid Polyoxometalates on Silicon. *Journal of*
7 *Materials Chemistry C* **2015**, *3* (24), 6266–6275. <https://doi.org/10.1039/C5TC00074B>.

8
9 (48) Mercier, D.; Boujday, S.; Annabi, C.; Villanneau, R.; Pradier, C.-M.; Proust, A.
10 Bifunctional Polyoxometalates for Planar Gold Surface Nanostructuration and Protein
11 Immobilization. *The Journal of Physical Chemistry C* **2012**, *116* (24), 13217–13224.
12 <https://doi.org/10.1021/jp3031623>.

13
14 (49) Huder, L.; Rinfray, C.; Rouchon, D.; Benayad, A.; Baraket, M.; Izzet, G.; Lipp-Bregolin,
15 F.; Lapertot, G.; Dubois, L.; Proust, A.; Jansen, L.; Duclairoir, F. Evidence for Charge Transfer at
16 the Interface between Hybrid Phosphomolybdate and Epitaxial Graphene. *Langmuir* **2016**, *32* (19),
17 4774–4783. <https://doi.org/10.1021/acs.langmuir.6b00870>.

18
19 (50) Vol.38 No.01 Pp.78-84 <https://www.jim.or.jp/journal/e/38/01/78.html> (Accessed Jul 19,
20 2019).

21
22 (51) Lombana, A.; Rinfray, C.; Volatron, F.; Izzet, G.; Battaglini, N.; Alves, S.; Decorse, P.;
23 Lang, P.; Proust, A. Surface Organization of Polyoxometalate Hybrids Steered by a 2D
24 Supramolecular PTCDI/Melamine Network. *The Journal of Physical Chemistry C* **2016**, *120* (5),
25 2837–2845. <https://doi.org/10.1021/acs.jpcc.5b11945>.

26
27 (52) Barr, T. L. An ESCA Study of the Termination of the Passivation of Elemental Metals. *The*
28 *Journal of Physical Chemistry* **1978**, *82* (16), 1801–1810. <https://doi.org/10.1021/j100505a006>.

29
30 (53) Dobson, K. D.; McQuillan, A. J. In Situ Infrared Spectroscopic Analysis of the Adsorption
31 of Aromatic Carboxylic Acids to TiO₂, ZrO₂, Al₂O₃, and Ta₂O₅ from Aqueous Solutions.
32 *Spectrochimica Acta Part A: Molecular and Biomolecular Spectroscopy* **2000**, *56* (3), 557–565.
33 [https://doi.org/10.1016/S1386-1425\(99\)00154-7](https://doi.org/10.1016/S1386-1425(99)00154-7).

34
35 (54) Zeleňák, V.; Vargová, Z.; Györyová, K. Correlation of Infrared Spectra of Zinc(II)
36 Carboxylates with Their Structures. *Spectrochimica Acta Part A: Molecular and Biomolecular*
37 *Spectroscopy* **2007**, *66* (2), 262–272. <https://doi.org/10.1016/j.saa.2006.02.050>.

38
39 (55) Caillard, L.; Sattayaporn, S.; Lamic-Humblot, A.-F.; Casale, S.; Campbell, P.; Chabal, Y.
40 J.; Pluchery, O. Controlling the Reproducibility of Coulomb Blockade Phenomena for Gold
41 Nanoparticles on an Organic Monolayer/Silicon System. *Nanotechnology* **2015**, *26* (6), 065301.
42 <https://doi.org/10.1088/0957-4484/26/6/065301>.

43
44 (56) Laurans, M.; Dalla Francesca, K.; Volatron, F.; Izzet, G.; Guerin, D.; Vuillaume, D.;
45 Lenfant, S.; Proust, A. Molecular Signature of Polyoxometalates in Electron Transport of Silicon-
46 Based Molecular Junctions. *Nanoscale* **2018**, *10* (36), 17156–17165.
47 <https://doi.org/10.1039/C8NR04946G>.

48
49 (57) Holmlin, R. E.; Haag, R.; Chabinye, M. L.; Ismagilov, R. F.; Cohen, A. E.; Terfort, A.;
50 Rampi, M. A.; Whitesides, G. M. Electron Transport through Thin Organic Films in
51 Metal–Insulator–Metal Junctions Based on Self-Assembled Monolayers. *J. Am. Chem. Soc.* **2001**,

1
2
3 123 (21), 5075–5085. <https://doi.org/10.1021/ja004055c>.

4
5 (58) Cui, X. D.; Zarate, X.; Tomfohr, J.; Sankey, O. F.; Primak, A.; Moore, A. L.; Moore, T.
6 A.; Gust, D.; Harris, G.; Lindsay, S. M. Making Electrical Contacts to Molecular Monolayers.
7 *Nanotechnology* **2002**, *13* (1), 5–14. <https://doi.org/10.1088/0957-4484/13/1/302>.

8
9 (59) Rampi, M. A., Whiteside, G. M. A Versatile Experimental Approach for Understanding
10 Electron Transport through Organic Materials. *Chem. Phys.* **2002**, *281*, 373–391.

11
12 (60) Wang, W.; Lee, T.; Reed, M. A. Mechanism of Electron Conduction in Self-Assembled
13 Alkanethiol Monolayer Devices. *Phys. Rev. B* **2003**, *68* (3), 035416.
14 <https://doi.org/10.1103/PhysRevB.68.035416>.

15
16 (61) Vilan, A. Analyzing Molecular Current-Voltage Characteristics with the Simmons
17 Tunneling Model: Scaling and Linearization. *J. Phys. Chem. C* **2007**, *111* (11), 4431–4444.
18 <https://doi.org/10.1021/jp066846s>.

19
20 (62) Simmons, J. G. Generalized Formula for the Electric Tunnel Effect between Similar
21 Electrodes Separated by a Thin Insulating Film. *Journal of Applied Physics* **1963**, *34* (6), 1793–
22 1803. <https://doi.org/10.1063/1.1702682>.

23
24 (63) Horiguchi, S.; Yoshino, H. Evaluation of Interface Potential Barrier Heights between
25 Ultrathin Silicon Oxides and Silicon. *Journal of Applied Physics* **1985**, *58* (4), 1597–1600.
26 <https://doi.org/10.1063/1.336046>.

27
28 (64) Krzeminski, C.; Delerue, C.; Allan, G.; Vuillaume, D.; Metzger, R. M. Theory of Electrical
29 Rectification in a Molecular Monolayer. *Phys. Rev. B* **2001**, *64* (8), 085405.
30 <https://doi.org/10.1103/PhysRevB.64.085405>.

31
32 (65) Dalla Francesca, K.; Lenfant, S.; Laurans, M.; Volatron, F.; Izzet, G.; Humblot, V.;
33 Methivier, C.; Guerin, D.; Proust, A.; Vuillaume, D. Charge Transport through Redox Active [H
34 ₇ P₈ W₄₈ O₁₈₄]³³⁻ Polyoxometalates Self-Assembled onto Gold Surfaces and Gold Nanodots.
35 *Nanoscale* **2019**, *11* (4), 1863–1878. <https://doi.org/10.1039/C8NR09377F>.

36
37 (66) Cardona, C. M.; Li, W.; Kaifer, A. E.; Stockdale, D.; Bazan, G. C. Electrochemical
38 Considerations for Determining Absolute Frontier Orbital Energy Levels of Conjugated Polymers
39 for Solar Cell Applications. *Adv. Mater.* **2011**, *23* (20), 2367–2371.
40 <https://doi.org/10.1002/adma.201004554>.

41
42 (67) Maeda, K.; Katano, H.; Osakai, T.; Himeno, S.; Saito, A. Charge Dependence of One-
43 Electron Redox Potentials of Keggin-Type Heteropolyoxometalate Anions. *Journal of*
44 *Electroanalytical Chemistry* **1995**, *389* (1–2), 167–173. [https://doi.org/10.1016/0022-0728\(95\)03872-E](https://doi.org/10.1016/0022-0728(95)03872-E).

45
46 (68) Vilan, A.; Cahen, D. Chemical Modification of Semiconductor Surfaces for Molecular
47 Electronics. *Chem. Rev.* **2017**, *117* (5), 4624–4666. <https://doi.org/10.1021/acs.chemrev.6b00746>.

48
49 (69) Ben M'Barek, Y.; Rosser, T.; Sum, J.; Blanchard, S.; Volatron, F.; Izzet, G.; Salles, R.;
50 Fize, J.; Koepf, M.; Chavarot-Kerlidou, M.; Artero, V.; Proust, A. Dye-Sensitized Photocathodes:
51 Boosting Photoelectrochemical Performances with Polyoxometalate Electron Transfer Mediators.
52
53
54
55
56
57
58
59
60

ACS Appl. Energy Mater. 2020, 3 (1), 163–169. <https://doi.org/10.1021/acsaem.9b02083>.

SYNOPSIS

